A Study of CINDY/DYNAMO MJO Suppressed Phase

SUE CHEN,* MARIA FLATAU,* TOMMY G. JENSEN,+ TOSHIAKI SHINODA,# JEROME SCHMIDT,* PAUL MAY,@ JAMES CUMMINGS,+ MING LIU,* PAUL E. CIESIELSKI,& CHRISTOPHER W. FAIRALL,** REN-CHIEH LIEN,++ DARIUSZ B. BARANOWSKI,## NAN-HSUN CHI,++ SIMON DE SZOEKE,@@ AND JAMES EDSON&&

* *Naval Research Laboratory, Monterey, California*
+ *Naval Research Laboratory, Stennis Space Center, Mississippi*
# *Texas A&M University, Corpus Christi, Texas*
@ *Computer Sciences Corporation, Monterey, California*
& *Colorado State University, Fort Collins, Colorado*
** *NOAA/Earth System Research Laboratory, Boulder, Colorado*
++ *University of Washington, Seattle, Washington*
Institute of Geophysics, Faculty of Physics, University of Warsaw, Warsaw, Poland
@@ *Oregon State University, Corvallis, Oregon*
&& *University of Connecticut, Groton, Connecticut*

(Manuscript received 4 October 2013, in final form 13 January 2015)

ABSTRACT

The diurnal variability and the environmental conditions that support the moisture resurgence of MJO events observed during the Cooperative Indian Ocean Experiment on Intraseasonal Variability (CINDY)/DYNAMO campaign in October–December 2011 are investigated using in situ observations and the cloud-resolving fully air–ocean–wave Coupled Ocean–Atmosphere Mesoscale Prediction System (COAMPS). Spectral density and wavelet analysis of the total precipitable water (TPW) constructed from the DYNAMO soundings and TRMM satellite precipitation reveal a deep layer of vapor resurgence during the observed Wheeler and Hendon real-time multivariate MJO index phases 5–8 (MJO suppressed phase), which include diurnal, quasi-2-, quasi-3–4-, quasi-6–8-, and quasi-16-day oscillations. A similar oscillatory pattern is found in the DYNAMO moorings sea surface temperature analysis, suggesting a tightly coupled atmosphere and ocean system during these periods. COAMPS hindcast focused on the 12–16 November 2011 event suggests that both the diurnal sea surface temperature (SST) pumping and horizontal and vertical moisture transport associated with the westward propagating mixed Rossby–Gravity (MRG) waves play an essential role in the moisture resurgence during this period. Idealized COAMPS simulations of MRG waves are used to estimate the MRG and diurnal SST contributions to the overall moisture increase. These idealized MRG sensitivity experiments showed the TPW increase varies from 9% to 13% with the largest changes occurring in the simulations that included a diurnal SST variation of 2.5°C as observed.

1. Introduction

The Madden–Julian oscillation (MJO) is a low-frequency atmospheric anomaly traveling along the equatorial belt with a period of 30–60 days (Madden and Julian 1971, 1972). The MJO has a broad influence on the weather and climate systems by influencing the intraseasonal and interannual variability of atmosphere and ocean (Lau and Waliser 2005; Zhang 2005). Numerous studies have characterized the large-scale environmental changes relative to MJO onset in terms of an increase in the boundary layer moisture near the central and eastern axis of the MJO convection and the development of westerly wind anomalies along the equator (Wang and Xie 1998; Kemball-Cook and Wang 2001; Weare 2003; Maloney and Hartmann 2000; Sperber 2003; Seo and Kim 2003). More recent studies (Tian et al. 2010; Benedict and Randall 2007) have shown the moisture distribution during the MJO cycle

Denotes Open Access content.

Corresponding author address: Sue Chen, Naval Research Laboratory, Marine Meteorology Division, 7 Grace Hopper Ave., Monterey, CA 93943.
E-mail: sue.chen@nrlmry.navy.mil

DOI: 10.1175/JAS-D-13-0348.1

consists of large-scale alternating dry and moist anomalies. Results from Benedict and Randall (2007) reveal a dry anomaly in the lower troposphere within 5 days of a MJO passage followed by large-scale subsidence throughout a deep layer of the troposphere 10–30 days after the passage. They indicate that a low-level positive moisture anomaly first reappears approximately 15 days prior to the onset of the MJO and is found to gradually build upward in time. The gradual moisture increase is accompanied by an increase in the westerly wind, warm temperature advection, and upward vertical velocity anomalies. This is in contrast to the more recent S-band radar analysis of Cooperative Indian Ocean Experiment on Intraseasonal Variability (CINDY)/Dynamics of the MJO (DYNAMO) cloud population by Powell and Houze (2013), which indicate a rapid increase in vapor occurring on a 1–2-day time scale. They show this was accompanied by a sharp increase in stratiform areal coverage prior to the onset of large-scale convection associated with each CINDY/DYNAMO MJO.

These results showing an increase in the moisture are supported by the analysis of stable hydrogen isotopic composition of H2O and HDO performed by Kurita et al. (2011) and Berkelhammer et al. (2012). Their isotopic analysis shows that the midtroposphere moisture source is derived from the evaporation of moisture from the ocean during the 15–20-day period prior to the MJO onset. During the MJO convective phase, the moisture source shifts from evaporation to a mixture of evaporation and horizontal convergence from the surrounding regions.

Many studies to date have focused on understanding the development of the positive moisture anomaly to the east of an active MJO. Theoretical frameworks developed to explain this attribute have included wave conditional instability of the second kind (CISK) (Lindzen 1974), modified wave CISK by strong thermal damping (Lau and Peng 1987), frictional wave CISK (Wang and Rui 1990; Seo and Kim 2003), extratropical waves (Hsu et al. 1990; Bladé and Hartmann 1993), the variability in sea surface temperature (SST) coupling (Flatau et al. 1997; Shinoda et al. 1998; Waliser et al. 1999), the discharge–recharge mechanism discussed by Hendon and Liebmann (1990) and Bladé and Hartmann (1993), large-scale horizontal moisture advection (Maloney 2009), and the moisture mode instability (Raymond and Torres 1998; Raymond and Fuchs 2009; Sobel and Maloney 2013). However, none of the aforementioned theories fully explain the transition from dry to moist regimes prior to the active MJO convection, nor do they offer insight as to what drives the formation of post-MJO shallow cumulus and deeper cumulus congestus clouds or whether these clouds by themselves are sufficient to increase the moist static energy needed to support the MJO initiation.

From the aforementioned studies, it is clear that the MJO initiation is a complex multiscale problem. The desire to improve the understanding and prediction of the MJO initiation has thus served as motivation for a special international field campaign, the Cooperative Indian Ocean Experiment on Intraseasonal Variability in the Year 2011 (CINDY2011)/DYNAMO that was held in the fall of 2011 to collect atmosphere and ocean data in the central Indian Ocean (Yoneyama et al. 2013). The goal of this paper is to utilize these unique datasets to investigate and improve our understanding of the processes impacting the deep moisture resurgence prior to the DYNAMO MJO initiation phase. What processes, for example, govern the time scale for the observed moisture resurgence in the post-MJO dry air mass prior to the subsequent MJO onset? What relative roles do diurnal ocean temperature anomalies and surface fluxes play in regulating or initiating the deep vapor resurgence? Do transient Kelvin, Rossby, mixed Rossby–gravity, and inertio-gravity waves impact the vapor resurgence?

We begin with a description of the data and modeling methods used in section 2. Analyses of observed in situ rawindsondes, surface flux, and sea temperature measurements from ship, moorings, and a glider are then presented in section 3 to establish the large-scale and mesoscale moisture environments of two MJO events. Section 4 compares results from real-time and hindcast model runs made with a nested, cloud-resolving, and fully coupled (air–ocean–wave) version of the Coupled Ocean–Atmosphere Mesoscale Prediction System (COAMPS). Here specific attention is given to an examination of the effect of air–ocean coupling on the interaction of large-scale mixed Rossby–Gravity (MRG) waves and local air–sea flux exchange. Detailed model results are presented in section 5 and include idealized COAMPS numerical experiments initialized with the horizontal and vertical structure of analytically derived MRG solutions. Such simulations are found to be useful in assessing the relative roles of diurnal SST heating cycle, air–sea interaction, and large-scale wave circulations on the moisture resurgence processes. A summary of the main findings can be found in section 6.

2. Methodology

a. Observational data

The core of DYNAMO sounding network consisted of six sites in the central Indian Ocean that formed the basis of two ship- and land-based sounding arrays located both north and south of the equator (Fig. 1). The best data coverage during DYNAMO occurred during

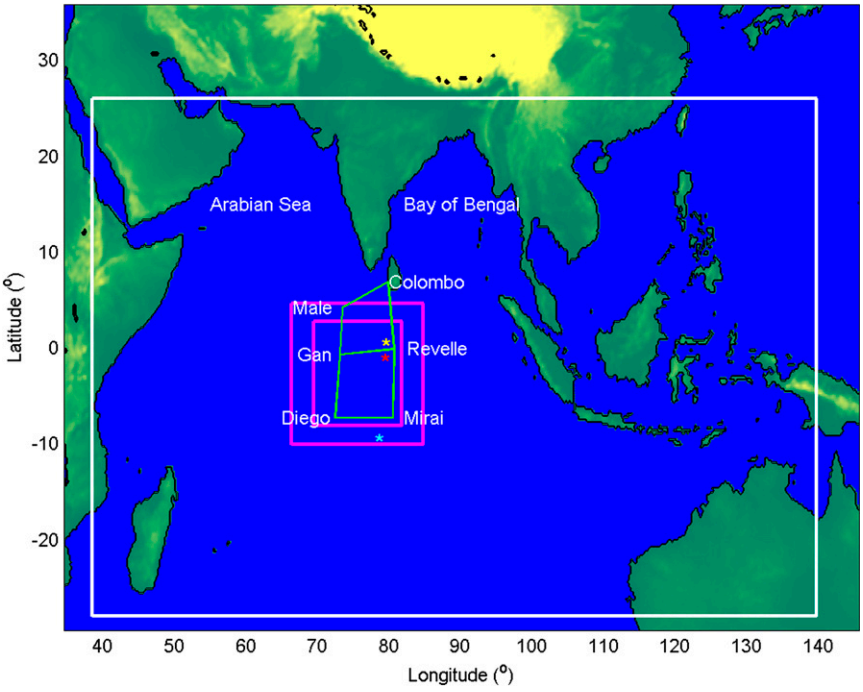

FIG. 1. Locations of CINDY2011/DYNAMO IOP sounding and mooring sites overlaid on the COAMPS atmospheric, ocean, and wave domains. The green box indicates the coverage area of the IOP array connecting the sounding sites Malé, Colombo, Gan, R/V *Revelle*, Diego Garcia, and R/V *Mirai*. The stars are the mooring sites D1 (yellow), D2 (red), and D3 (cyan). The inner-two atmospheric grids are shown as magenta rectangles, and the ocean and wave model grid is shown in white. The 3-km atmospheric nest 3 covers an area of 8.1°S–2.8°N and 69.5°–81.9°E°.

the special observing periods (SOP) when sites in the southern sounding array (SSA) launched eight sondes per day and the two northern sounding array (NSA) sites Malé and Colombo launched four sondes per day. The DYNAMO soundings and dropsondes were assimilated into the operational models including COAMPS. The real-time soundings contained a small daytime dry bias on the order of a few percent relative humidity (RH) at low levels and increased to ~5% at upper levels. Soundings subsequently processed for the analyses presented in this paper used level 4 (L4) processed sonde data, which are quality controlled and bias corrected (Ciesielski et al. 2012).

The Earth System Research Laboratory (ESRL) direct covariance flux system contains infrared hygrometers, downwelling longwave and shortwave pyranometers, RH–temperature–pressure sensors, rain gauge, and floating SST. The SST has been corrected for the cool skin. The 10-m temperature, wind speed, humidity, and the bulk fluxes of wind stress, sensible heat, and latent heat are estimated from the COARE 3.0 algorithm (Fairall et al. 2003). The wind speeds relative to water are used to compute the bulk fluxes. Table 1 summarizes all other observational datasets that were of particular interest in this study, including three moorings from the University of Washington; *Revelle* conductivity–temperature–depth (CTD) profiler provided by Oregon State University; autonomous underwater vehicles (sea glider) from the University of East Anglia, United Kingdom; TRMM-3B42 from the National Aeronautics and Space Administration (NASA); and *Meteosat-7* from the European Space Agency. A more complete list of CINDY2011/DYNAMO observations is available in Yoneyama et al. (2013).

b. *Spectral analysis and wave filtering*

The diurnal and large-scale wave-induced oscillations in both the atmosphere and upper ocean are inferred from the time series analysis of power spectral density (PSD) and wavelet analysis of observed variables such as the NASA TRMM-3B42 TRMM precipitation (http://disc.sci.gsfc.nasa.gov/precipitation/documentation/TRMM_README/TRMM_3B42_readme.shtml), total precipitable water (TPW) obtained at each of the six sounding sites, and the SST observed at the three DYNAMO moorings. Wavelet analysis is useful because it provides

TABLE 1. A list of CINDY/DYNAMO in situ and satellites products used in this study.

Observation data type	Data frequency
Rawinsondes	3 hourly
Air–sea flux	1 hourly
Revelle CTD	12 hourly
Moorings (CTD and ADCP)	1 hourly
Sea gliders	1 hourly
TRMM-3B42	3 hourly
METEOSAT7	30 min

both an estimate of the power as well as the timing of the individual peaks. Tests of the statistical significance of individual peaks in the power spectra and wavelet analyses were assessed against the red-noise spectrum at 95% confidence level following the method of Torrence and Compo (1998).

The TRMM data were also used to identify the atmospheric large-scale waves by applying the space–time FFT filtering technique (Yang et al. 2003; Roundy 2008). This technique is also well known to provide an ability to separate the signals associated with the eastward (Kelvin, MJO, eastward MRG, and eastward inertio-gravity waves) and westward (equatorial Rossby, westward MRG, and westward inertio-gravity) propagating waves. The advantage of using TRMM precipitation is that the dataset contains only the convectively coupled waves. A 2D FFT is applied to transform the data to time and wavenumber space. The eastward- and westward-moving waves are obtained by filtering the 10°S–10°N latitude banded TRMM data to retain the zonal wavenumbers 1–14 and periods of 2–20 days (Wheeler and Kiladis 1999).

c. Description of COAMPS model

The development of a fully coupled COAMPS spans over a decade of work starting from the initial atmospheric component discussed by Hodur (1997) and Chen et al. (2003) and has since been updated with a fully two-way air–ocean–wave coupled system using the Earth System Modeling Framework (ESMF; Chen et al. 2010; Jensen et al. 2011; Small et al. 2011; Smith et al. 2013). For this study, Simulating Waves Nearshore (SWAN) is used with 0.25° horizontal resolution, 36 directions, and 33 frequencies. The nonhydrostatic atmospheric component was set up to run with three horizontal grids (with a horizontal grid spacing of 27/9/3 km, respectively) and 60 vertical sigma levels wherein 20 levels were assigned within the lowest 2 km of the atmosphere. The Navy Coastal Ocean Model (NCOM; Martin 2000) is run using a horizontal resolution of 12 km with 60 sigma-z vertical layers. A fine vertical spacing (0.5 m) is used in the upper 10 m to resolve the large diurnal warming features (Shinoda et al. 2013). The vertical mixing is modified to include Stokes drift currents provided by a wave model and effects of Langmuir circulations (Smith et al. 2013).

d. COAMPS real-data simulations

During the CINDY2011/DYNAMO campaign, a research version of the fully air–ocean–wave coupled COAMPS provided real-time forecast support for the field campaign. COAMPS used a 6-hourly data assimilation cycle in the atmosphere and ocean from 17 August 2011 to 15 January 2012 and issued a 4-day forecast once a day at 1200 UTC. The atmospheric coarse domain covers the area of 25°S–25°N and 30°–150°E while the 3-km atmospheric nest was designed to encompass the entire CINDY2011/DYNAMO southern sounding array, covering an area of 8.1°S–2.8°N and 69.5°–81.9°E (Fig. 1). The ocean and wave domain are the same size and slightly smaller than the atmospheric coarse domain.

The MJO real-time multivariate (RMM) index phases 5–8 (Wheeler and Hendon 2004) are chosen to provide a definition of MJO suppressed phase used in the following discussions. Following Powell and Houze (2013, their Table 1), the corresponding dates for the MJO RMM index phases 5–8 during CINDY/DYNAMO period are 1–14 October, 6–16 November, 6–12 December, and 29 December to 9 January. The focus of this study is to investigate the moisture resurgence processes during the suppressed phase prior to the November MJO that covers a 4-day period between 12–16 November (~10 days prior to the MJO2 initiation in the DYNAMO array). The coupled hindcast simulations consist of a three-component (air–ocean–wave), six-way fully coupled run using the initial and boundary conditions from the real-time COAMPS run at 0000 UTC 12 November 2011. The *Revelle* CTD, glider, and DYNAMO moorings were not assimilated in COAMPS real-time forecasts. The impact of air–sea interaction and the role of diurnal cycle are investigated using the uncoupled experiment, which has the same initial and boundary condition as the coupled hindcast forecast except that the spatially varying initial SST analysis is held constant throughout the forecasts.

e. COAMPS idealized simulations

Idealized dry and convectively coupled MRG wave simulations are conducted using COAMPS in an effort to obtain qualitative estimates of their contributions to the moisture resurgence during the MJO suppressed phase. The horizontal grid resolution for these experiments was set to be 0.5° using a spherical grid projection centered on the equator that spanned 140° longitude and 60° latitude. The lateral boundary conditions were set

to be periodic in the east–west direction and radiative along the northern and southern grid boundaries. The MRG perturbation fields were derived from the analytical expressions determined from Eqs. (11-28) through (11-42) of Holton (1979, 308–311). These perturbations were superimposed on a horizontally homogeneous mean state consisting of quiescent flow conditions and a vertical potential temperature profile consisting of a constant Brunt–Väisälä frequency ($N = 0.012\,s^{-1}$). The initial vertical distribution of the water vapor was derived from the 12–19 November sounding composite taken from Gan. We utilized the digital filter method of Lynch and Huang (1992) for a period of 8 h (4 h forward and 4 h backward time integration) to produce an initial vertical velocity that was consistent with the initial perturbed temperature and wind fields. The control experiment (EXPA) was then run forward for an additional 96 h using the dry dynamics and a limited set of model physics that include the surface fluxes and turbulence vertical mixing operating on all scalars and the model momentum variables. The dry MRG was specified to have a horizontal wavelength of 8000 km and a vertical wavelength of approximately 6 km. The frequency was chosen to produce a westward propagating wave with a phase speed of $17\,m\,s^{-1}$. The MRG wave setup is within the theoretical and observed MRG parameter space discussed by Matsuno (1966), Hendon and Liebmann (1991), and Yasunaga et al. (2010). The magnitude of the horizontal velocity perturbations at the surface was set to a value of $5\,m\,s^{-1}$. Two ideal sensitivity studies were initialized and run in a similar manner except that they include a time-varying SST anomaly (EXPB) and a fully physics run (EXPC) that has both the SST anomaly, the COAMPS single-moment bulk microphysics scheme, and the simplified Arakawa–Shubert cumulus scheme activated (Pan and Wu 1995). The initial SST in all experiments was set to a constant value of 30°C. The diurnal cycle in the two sensitivity runs is imposed with a peak 2.5°K half sine wave structure ($\Delta SST \geq 0$) in an effort to mimic the SST observations from CINDY/DYNAMO shown later in section 4. Table 2 lists the idealized experiment model setup.

TABLE 2. A list of idealized COAMPS mixed–Rossby gravity wave experiments.

Experiment name	Model setup
EXPA	Dry with fixed SST
EXPB	Dry with time-varying SST
EXPC	Full physics with time-varying SST

3. Observed atmosphere and ocean conditions during October–December 2011

Three DYNAMO MJO events were observed during the October–December 2011 timeframe with the first two separated by a 30-day time span between October and November 2011 (Yoneyama et al. 2013). These events are readily identified from the eastward propagating convective signature of the Kelvin wave filtered TRMM rainfall in the CINDY2011/DYNAMO array (Fig. 2). During the MJO suppressed phase, the atmospheric conditions within the CINDY2011/DYNAMO array consisted of a mixture of conditions including isolated deep convection, shallow nonprecipitating clouds, weak winds, and vast clear air regions as ascertained from the Meteosat (https://www.eol.ucar.edu/field_projects/dynamo) infrared and visible observations. This diversity is reflected in the considerable variability in the time series analyses of the vertical relative humidity (herein referred to as RH) structure obtained from all six DYNAMO sounding sites. The larger-scale drying and moistening associated with the post-MJO and MJO periods are evident in the plot as are a number of smaller temporal fluctuations occurring on variety of time scales (Fig. 3). A rapid falloff in the RH values through a deep layer of the troposphere in the post-MJO environment in Fig. 3 is near 9 October, 5 November, 30 November, and 28 December, for example, in both the equatorial soundings at *Revelle* and Gan. Inspection of individual soundings taken during the suppressed phase of the first two MJO cases further reveal the base of the dry layer extends to as low as 800 hPa with sharp increases in the dewpoint depression above that level that were maintained throughout the depth of the troposphere (not shown). The RH appears to build upward from levels just above the boundary layer prior to MJO onset as noted to occur in previous composites (Benedict and Randall 2007) with some evidence of both westward and eastward tilt with height of individual RH maxima (such as the westward tilt with height in some of the RH filaments in mid-October at *Mirai* and Colombo). The minimum and maximum TPW values during the larger-scale drying and moistening oscillations at sites such as *Revelle* (Gan) are approximately 40.13 (41.02) mm and 70.59 (66.91) during October and November, respectively (Fig. 4). The least squares fit of the data gives the moistening rate of 0.0576 and $0.2120\,mm\,day^{-1}$ 10 days prior to the initiation of MJO1 and MJO2 at *Revelle*, respectively, suggesting that the moisture resurgence rate prior to MJO2 was greater than that of MJO1. While other sites indicated readily identifiable trends in TPW as well (such as at Colombo) this was by no means a universal feature as stations such as Diego Garcia (Fig. 3) experienced more

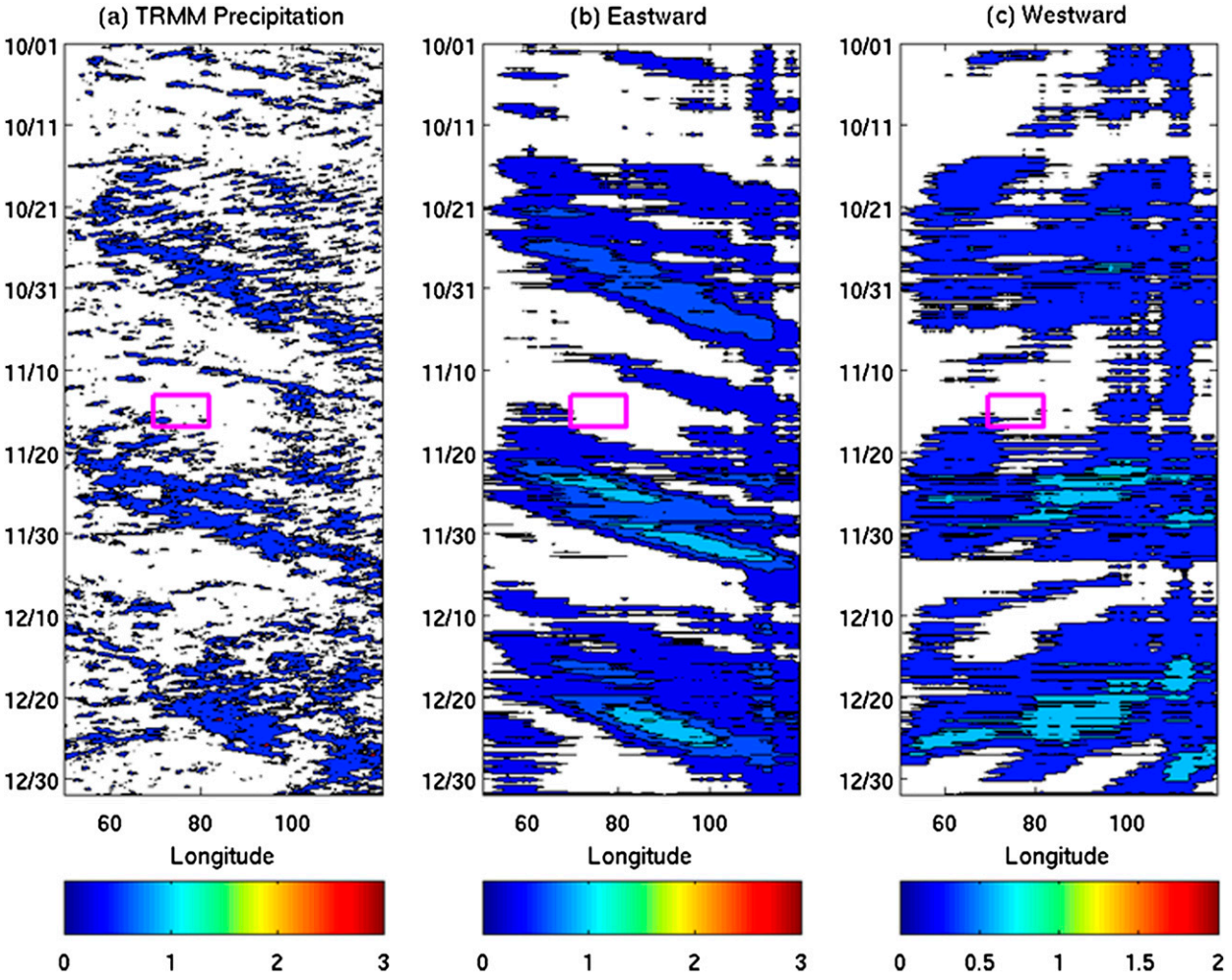

FIG. 2. (a) Time–longitude Hovmöller diagram of TRMM-3B42 3-hourly precipitation band averaged multisensor satellite rain rate analysis (shaded) between 10°S and 10°N. (b),(c) As in (a), except for the eastward propagating and westward propagating modes, respectively. The contour interval is 0.3 mm h^{-1}. The zero contours are not plotted. The magenta box represents the 12–16 Nov time period and 70°–82°E, which is the longitudinal range of the COAMPS grid-3 domain in Fig. 1.

frequent and briefer episodic surges related to fluctuations in the ITCZ convection (Johnson and Ciesielski 2013).

The nature of the higher temporal variability in Fig. 3 and Fig. 4 is more clearly revealed through a plot of the October–December PSD and wavelet analysis of TPW from the DYNAMO soundings shown in Fig. 5. The spectral analysis of the sounding TPW time series reveals spectral peaks on quasi-2-, quasi-3–4-, quasi-6–8-, and quasi-16-day oscillation periods. All peaks from the PSD analysis in six sounding sites exceed that of the red-noise spectrum while several sites have statistically significant peaks at or exceeding the 95% level. The 3–4-day peaks, for example, exceed the 95% confidence level at all sounding sites except at *Revelle*, while only Diego shows a statistically significant peak at the 95% level in the 6–8-day range. Because the *Revelle* has data gaps during its port call in late October and mid-December, its PSD and wavelet analysis is less reliable than at other sites. An independent check using the TRMM rain (not shown) indicates similar spectral peaks exceeding that of the background red-noise spectra in the 2-, 3–4-, 6–8-, and 16-day periods. Of these, however, only Diego exhibited 3–4- and 6–8-day PSD peaks exceeding the 95% confidence level.

Interestingly, the wavelet analysis of the TPW anomaly time series reveals the 3–4-day peaks occurred in the MJO suppressed phase as well as during the MJO initiation. The exact times of these 3–4-day wavelet peaks occurred varied widely among these six stations. All sites have the 3–4-day wavelet spectrum peaks that exceed the estimated background red-noise spectra

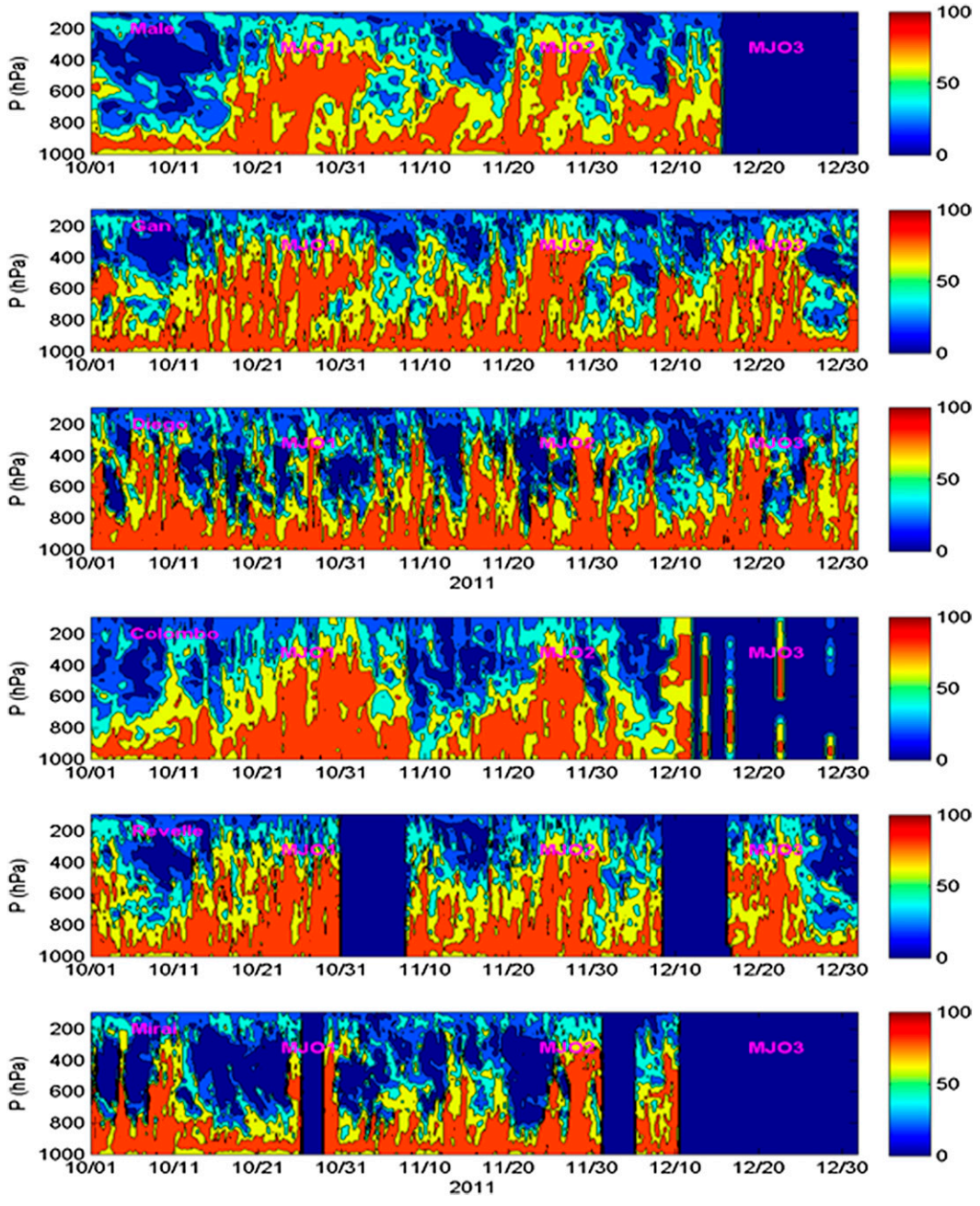

FIG. 3. Time–height relative humidity [with respect to liquid water (%)] analysis derived from observed soundings at Malé (4.2°N, 73.5°E), Gan (0.69°S, 73.15°E), Diego Garcia (7.3°S, 72.4°E), Colombo (6.91°N, 79.87°E), *Revelle* (0.1°N, 80.6°E), and *Mirai* (8.01°S, 80.51°E). The contour interval is 20% and the three primary MJO's arising during this period are labeled in magenta.

during the suppressed phase of each of the three MJOs. The wavelet spectrum peaks that are statistically significant at the 95% level (red contours in Fig. 6–7) are observed at *Mirai* between 1 and 14 October, at Colombo between 6 and 16 November, and at Malé between 6 and 12 December. The 6–8-day wavelet spectrum peaks that are statistically significant also occurred in the MJO suppressed phase at different sounding sites.

The derived characteristics in the TPW and rain PSD and wavelet spectrum shown in Figs. 5–7 resemble the 3–4- and 6–8-day disturbances that were observed during the *Mirai* Indian Ocean Cruise for the Study of the MJO

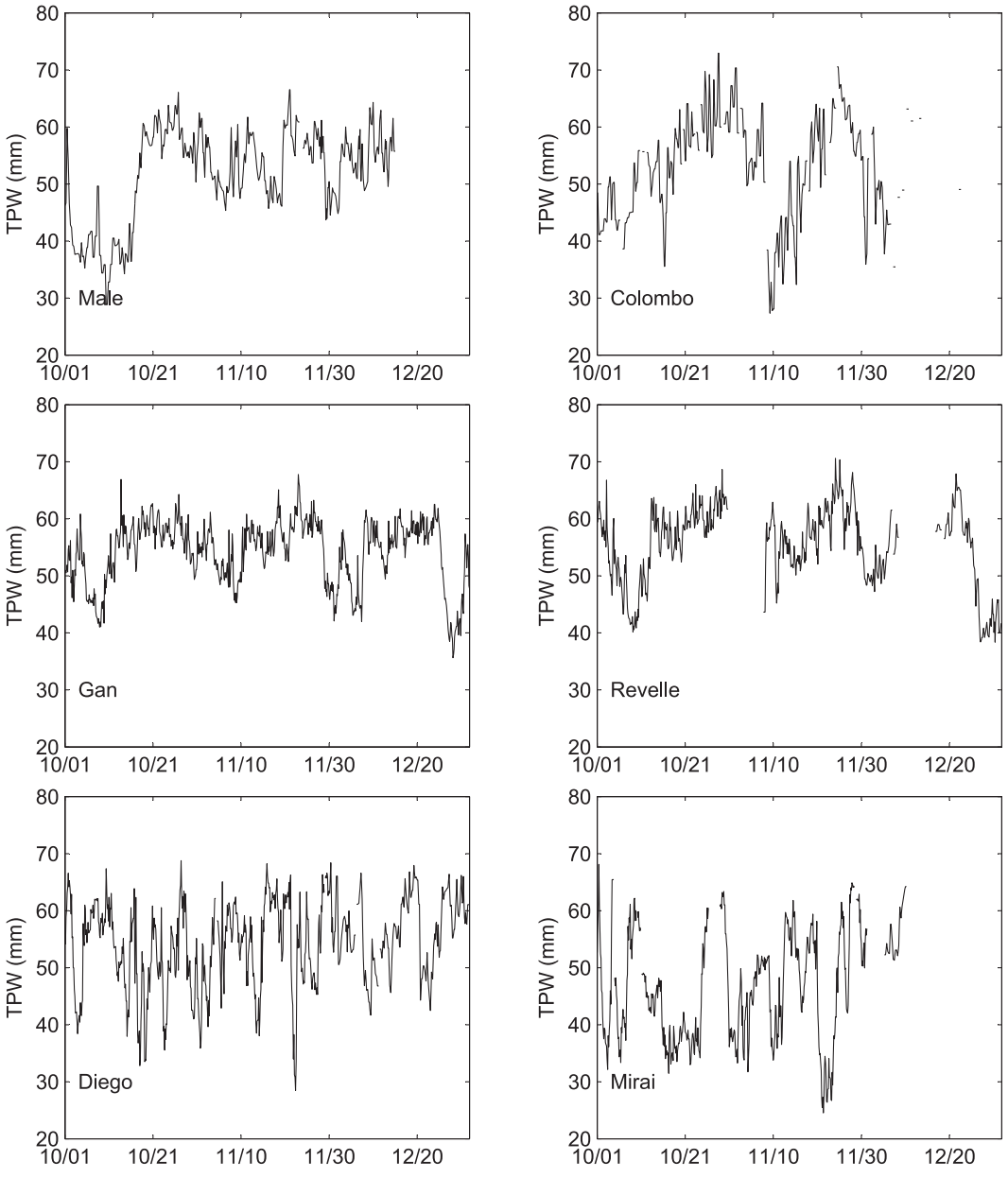

FIG. 4. Total precipitable water (mm) vs time computed from the 3-hourly DYNAMO L4 soundings at Malé, Gan, Diego Garcia, Colombo, RV *Revelle*, and R/V *Mirai*.

Onset (MISMO) in October 2006 (Yasunaga et al. 2010). In their case, they found that the characteristics of the 3–4-day westward propagating disturbances were consistent with those associated with MRG waves while the longer oscillations on the order of 6–8 days were related to $n = 1$ equatorial Rossby waves. Other observations show the westward propagating MRGs and Rossby have a wide range of values in the oscillation period (Kiladis et al. 2009). The range of the MRG periods is from 3 to 6 days and 6 to beyond 20 days for $n = 1$ Rossby waves. The quasi-2-day peaks have been suggested to be associated with the inertio-gravity waves (Johnson and Ciesielski 2013; Takayabu et al. 1996).

Further details of the oscillatory nature of the moisture and precipitation field associated with these MJO events are obtained from the TRMM Hovmöller diagram (Fig. 2a) constructed between 10°S and 10°N for the eastward (Fig. 2b) and westward (Fig. 2c) moving waves. Oscillations in the dry–moist moisture cycle were found to precede each MJO initiation. The quasi-3–4-day

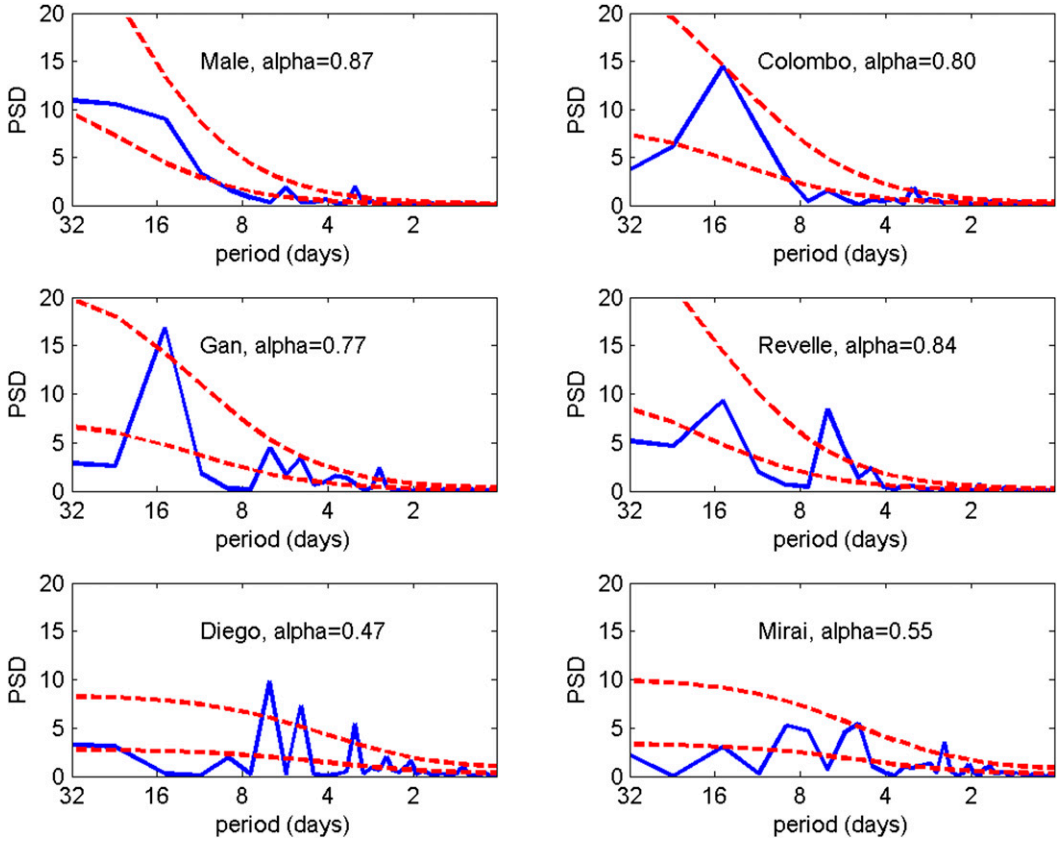

FIG. 5. Normalized power spectral density of total precipitable water derived from the sounding sites shown previously in Fig. 4. The lower dashed line is the red-noise spectrum. The upper dashed line is the 95% confidence red-noise spectrum. Alpha is the value of the lag-1 autocorrelation.

oscillations shown in Fig. 2c are suggestive of westward propagating MRG waves similar to those found by Yasunaga et al. (2010). Accompanying these fluctuations in the TPW and precipitation were similar oscillations in the sea surface temperature anomalies (Fig. 8). The 3-hourly SST values observed from the three DYNAMO moorings (D1–D3) between October and December generally show a gradual fluctuation in the SST trend on the MJO time scale at the two equatorial moorings (D1 and D2). They also show the SST warming preceding the MJO1 and MJO2 initiation and a rapid cooling during the MJO convection phase. The SST PSD analysis shows the SST oscillation at D2 and D3 on a diurnal and quasi-2-, quasi-3–4-, quasi-6–8-, and quasi-16-day time scale. These quasi-2- and quasi-3–4-day SST oscillations are statistically significant at the 95% level at D2 and D3. They have about the same time scale as the atmospheric PSD peaks of TPW from the soundings and precipitation from TRMM. This suggests a possible linkage between these aforementioned features through the air–sea coupling, which we explore further in the next two sections using model-based data derived from COAMPS.

4. Verification of COAMPS simulated moisture structure, air–sea fluxes, and ocean temperature structure

The ability of COAMPS to represent the Indian Ocean MJO structures such as indicated above has previously been established for a number of springtime events examined by (Shinoda et al. 2013). Comparisons of the model structure with the falltime events occurring during CINDY2011/DYNAMO moisture soundings are demonstrated here to also produce reasonable agreement with the available observations during both the initiation and evolution of MJO1 and MJO2. This is initially demonstrated in Fig. 9, which shows the comparison of the real-time COAMPS 6-h forecasts of TPW from 1 October to 30 November 2011 at the *Revelle*, Gan, and Diego Garcia sites. Compared to the DYNAMO soundings, COAMPS is seen to underestimate the amount of moisture in the atmosphere during both the onset of MJO1 and MJO2 but has better agreement with all three sounding stations in the time period preceding the MJO2 initiation. In the suppressed

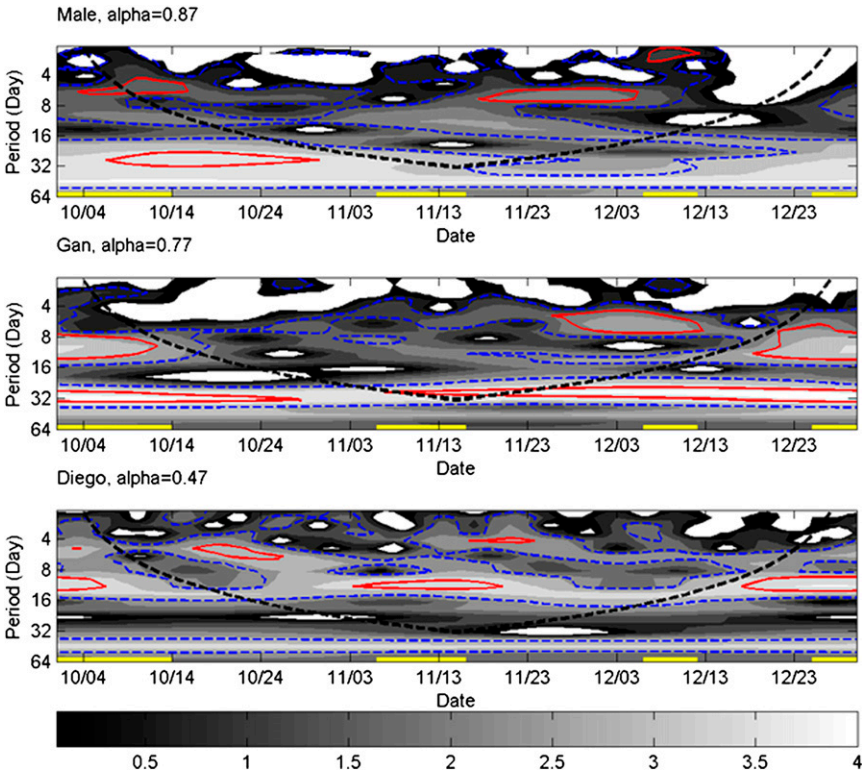

FIG. 6. The local wavelet power spectrum of the total precipitable water at (top to bottom) Malé, Gan, and Diego Garcia. The shaded regions are the normalized wavelet power spectrum. The blue dashed contours are for regions of greater than a red-noise process. The red contours are for regions of greater than 95% confidence for a red-noise process with a lag-1 autocorrelation alpha. The yellow bars represent the periods of Wheeler and Handen MJO index phases 5–8 (see Table 1 from Powell and Houze 2013). The black dashed line indicates the cone of influence, where edge effects of the time series become important.

phase of 12–16 November, the 4-day forecast mean overestimates the TPW by 2.2 mm compared to the *Revelle*, Gan, and Diego Garcia soundings (not shown).

A comparison of the model hindcast fields interpolated in time and space to the *Revelle* location shows good quantitative agreement with the *Revelle* observations over a 93-h period for selected 10 parameters illustrated in Fig. 10. The primary exceptions to this general statement are the short-lived transient spikes in the rain and longwave (LW) radiation associated with the modeled convection. Overall, the COAMPS SST maxima lag the observations by a few hours but the peak magnitude of the COAMPS SST is closer to that of the observed near-surface SST (Fig. 10). The maximum and minimum near-surface SST from the *Revelle* are 29° and 31.5°C on 13 November, respectively, giving observed maximum diurnal SST amplitude of approximately 2.5°C. The Revelle (model) mean wind speed is 2.3 (2.5) m s^{-1}, while the mean sensible and latent heat fluxes are 5.3 (5.1) and 82.4 (105.6) W m^{-2}, respectively (Fig. 10). The surface net shortwave radiation (SW) is about 268.7 (287.5) W m^{-2} and LW is 60 (41.9) W m^{-2} (Fig. 10). During 12–16 November, a 3 mm h^{-1} precipitation event is observed on the fourth day (15 November) at 1400 local time (0900 UTC). Unlike the observations, the COAMPS forecast has two 2–3 mm h^{-1} rain events on days 1 and 3 in the late afternoon that are associated with a corresponding drop in the 10-m temperature and relative humidity values and an increase in the sensible and latent heat fluxes and wind speed (Fig. 10).

The largest model error occurs in the upward surface LW where the mean COAMPS net upward LW is about 18 W m^{-2} less than the observations. The COAMPS fluxes deficit result in an increase in the net flux of heat to the ocean of about 6 W m^{-2} during daytime and less outgoing flux to cool the ocean at night (Fig. 10j). The model SST phase error may cause a reduction in the rate of the vertical mixing in the ocean layer compared to the real ocean mixing processes and thus some overestimate in the strength of daytime convection may have arisen at the *Revelle* location.

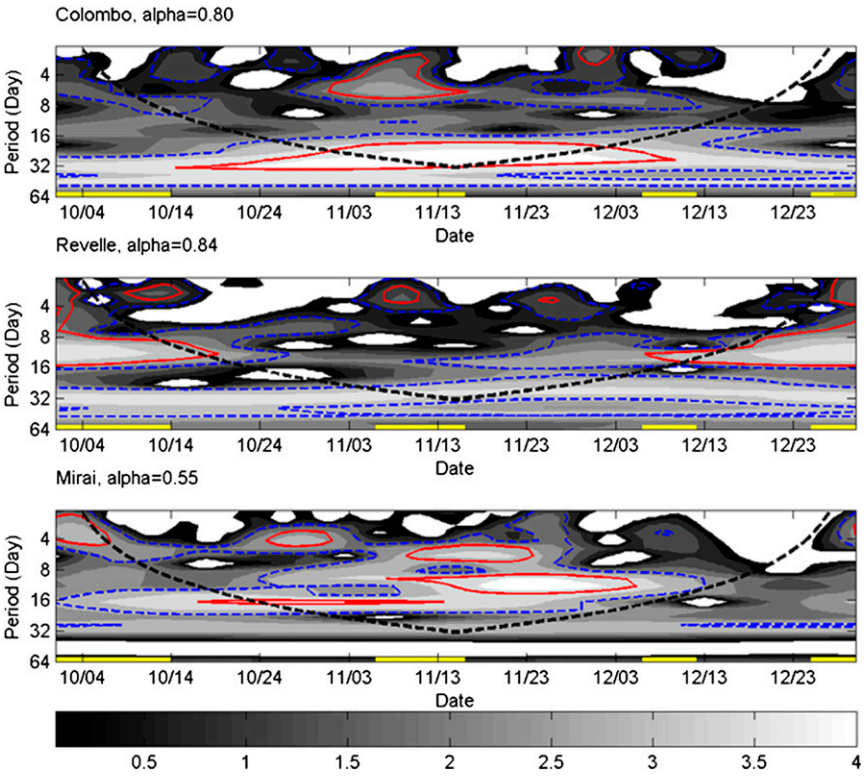

FIG. 7. As in Fig. 6 except for Colombo, R/V *Revelle*, and R/V *Mirai*.

The storage of heat in the ocean under clear-sky conditions in the MJO suppressed phase is important for the subsequent discharge rate of energy from the ocean into the atmosphere during the active phase of the MJO. The COAMPS vertically averaged ocean temperature from the surface to 80-m depth ($T_{\overline{80}}$) and mixed layer depth (MLD) during the 4-day forecast on 12 November is compared with the *Revelle* shipboard CTD, DYNAMO moorings, and the sea glider, which is near 3.4°S, 78.7°E (Fig. 11). The weighted-depth-averaged temperature shown can be used as a proxy that relates the heat storage to the vertical mixing in the upper ocean (Price 2009). The *Revelle* CTD observations indicate that strong turbulent mixing occurred in the upper 50–80 m of the ocean in October and November (Yoneyama et al. 2013). Therefore, $T_{\overline{80}}$ is used instead of the value typically used to examine the ocean heat content (OHC) in the hurricane environment ($T_{\overline{80}}$). The mixed layer thickness is calculated based on the depth where the density jump is equivalent to a 3°C temperature change from the 2-m height while holding the salinity constant at the 2-m-level value. These criteria give a shallower MLD but capture the daytime diurnal warm layer and avoid the problem of missing salinity data in the upper 1 m of ocean from the sea glider.

Both the observations and model show considerable spatial and temporal variability in the $T_{\overline{80}}$ and MLD but a smaller model $T_{\overline{80}}$ variation is seen at D1, D2, and Glider locations. The mean $T_{\overline{80}}$ at *Revelle*, D1, D2, and the glider are 29°, 28.7°, 28.7°, and 27.9°C, respectively, while the MLD is 8.2, 9.94, 12.78, and 15.4 m, respectively. Compared to the observations, the COAMPS mean $T_{\overline{80}}$ bias and RMS at these four locations are 0.3° and 0.5°C, respectively, while the MLD (model − obs) stands at −1.8 and 5.9 m, respectively. In general, the COAMPS $T_{\overline{80}}$ value is higher while the MLD is shallower than observations but the differences are small. The lack of an upper-0.5-m temperature measurement from the sea glider also contributed to the differences between COAMPS and the observations. The combination of negative OHC and MLD bias might affect the transfer rate of energy from the ocean to the atmosphere through changes of SST. Nevertheless, similar to the TPW, COAMPS OHC and MLD errors are small compared to the observations. These validation statistics therefore provide credence to the model results and thus form a basis for the interpretation of COAMPS model results in regard to the moisture resurgence processes described in the following sections.

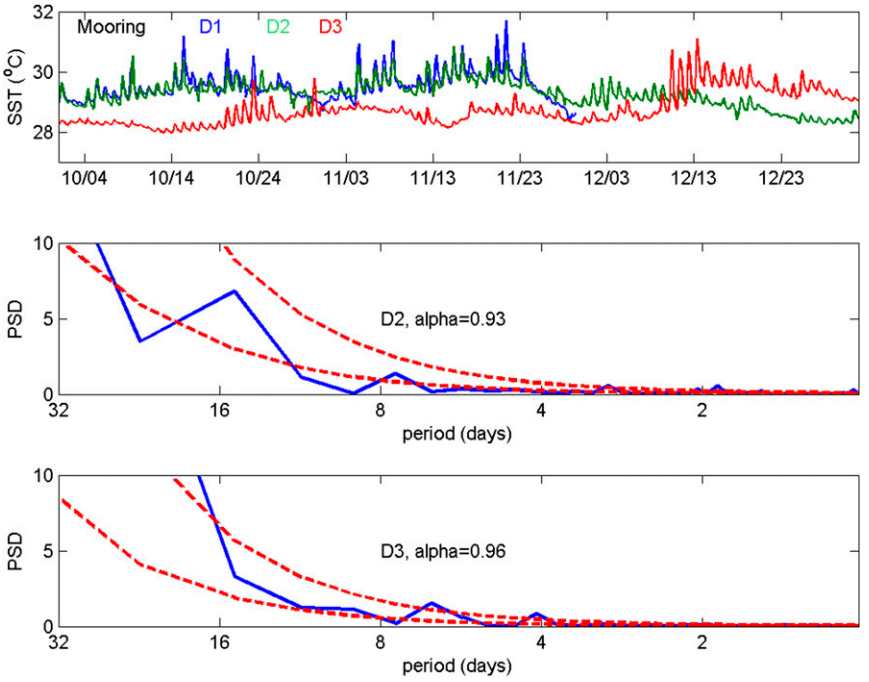

FIG. 8. (top) Three-hourly SST (°C) from the DYNAMO moorings D1, D2, and D3 and their normalized PSD analysis. The PSD from the (middle) D2 and (bottom) D3 moorings show 2-, 3–4-, 6–8-, and 16-day oscillations. The lower dashed line is the red-noise spectrum. The upper dashed line is the 95% confidence red-noise spectrum. Alpha is the value of the lag-1 autocorrelation. The positions of the moorings are indicated in Fig. 1. D1 was vandalized near 20 Nov so no measurements were made at 1 m and above after that date.

5. COAMPS simulations during 12–16 November

a. Real-data simulations

COAMPS model simulation results from the innermost domain (see Fig. 1) are shown for 12–16 November to illustrate the structures obtained during the suppressed phase leading up to the second MJO. The time–longitude Hovmöller plot in Fig. 2c and the wavelet spectrum analysis suggests that this period coincided with the passage of westward moving convectively coupled MRG waves through the eastern portion of the CINDY2011/DYNAMO array. The Rossby wave in this period is not present in the analysis of Gottschalck et al. (2013, their Fig. 13) and also absent in most of the DYNAMO sounding wavelet analysis. A sequence of Meteosat water vapor images taken over the Indian Ocean during this period (Fig. 12) reveals several westward moving clusters of enhanced convection that appear to alternate in an asymmetric pattern about the equator (labeled A–D) in a manner suggestive of a MRG disturbance (Kiladis et al. 2009). The convective region labeled C impacts the northern COAMPS domain between 10 and 12 November before decaying as it moves west of the area by 13 November. Isolated convective elements in this cluster are likely responsible for the intermittent higher-valued RH plumes of varying depth that are interspersed within general dry layer found aloft at this time (Fig. 3). The domain remains relatively free of deep convection after this cluster until a more pronounced region of convection (labeled D) impacts the middle-to-southern portion of the domain between 13 and 16 November. This second feature produced similar impacts on the sounding RH structure over the southern sounding sites and led to an upward trend in the areal coverage and depth of the convection over the COAMPS domain that continued up to the initiation of the MJO2 on 23 November.

The COAMPS hindcast experiment initiated at 0000 UTC 12 November captures the overall evolution of the observed general trends in the suppressed phase preceding MJO2 quite well. As in the observations, the COAMPS forecast on 12 November started with several isolated convective cells over the northern portion of the domain with a trend toward more convection of the entire domain in time (Fig. 13). Such evolution is a common attribute for a variety of convectively coupled wave types as reviewed by Kiladis et al. (2009). Here this sequence corresponded with a gradual shift in the winds to an easterly flow component over the entire domain as well as pronounced changes in the underlying SST

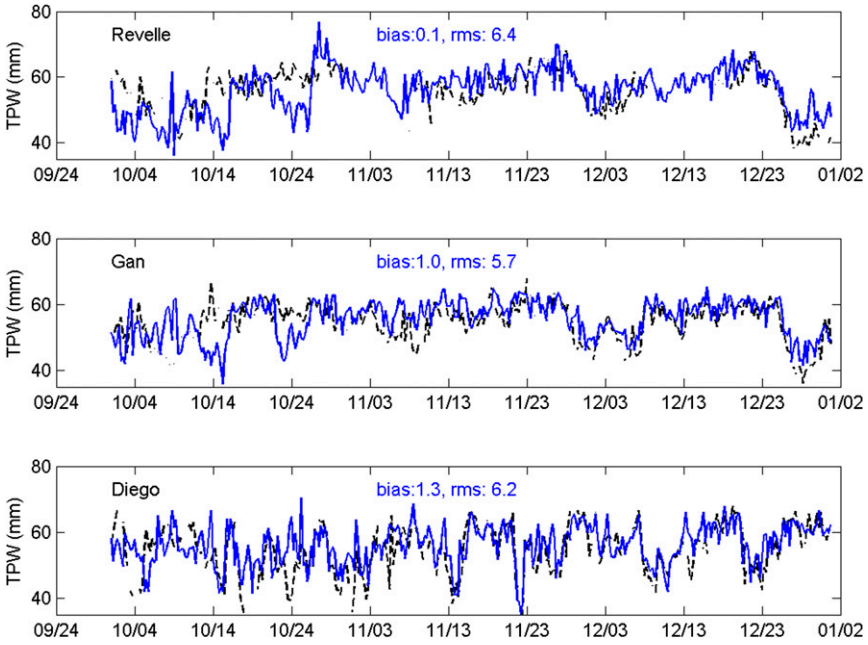

FIG. 9. Comparison of COAMPS (blue) and the (top) *Revelle*, (middle) Gan, and (bottom) Diego Garcia total precipitable water (mm) between 1 October and 31 December 2011. Any small temporal gaps in the COAMPS profile resulting in missing real-time forecast runs were filled with the fields available from the previous forecast valid at the same time.

structure. These SST variations were associated with both the solar heating cycle and convectively generated cold pools that induced vertical mixing in the ocean due to enhanced surface wind stress in regions of convective outflow.

Intense daytime solar heating led to higher domain mean SST values and the eventual erosion of the cold convectively induced SST pockets produced during the previous night. Plots of selected 10 mean model parameters suggest that the boundary layer recovery accompanying the warmer daytime SSTs was associated with deeper and more vigorous convection than found to occur during the nighttime hours. This is particularly noticeable during the first 2 days of the simulation when most of the area within grid 3 is cloud free and the environment is therefore more likely to be dominated by strong diurnal heating of the SST. In particular, we find that the peak values in the mean kinetic energy, enthalpy, low-level convergence (obtained over the lower 30–50 m), and rainfall shown in Fig. 13 all tend to lag the period of peak daily SST heating within approximately 3–7 h (Fig. 14). For example, the SST and SST gradient [defined here as the mean absolute magnitude of the Laplacian of the SST (°C $9\,km^{-2}$) following Li and Carbone (2012)] are almost in phase with a lag correlation coefficient of ~0.9, and the SST and rainfall has a 7-h lag with a lag correlation coefficient of ~0.5.

The lag in the low-level convergence is interesting and may be related to either a direct response of the low-level flow to changes in the overall magnitude of the SST or from known boundary layer processes that act to increase the low-level convergence in the presence of a stronger SST gradient such as noted by Frenger et al. (2013), O'Neill et al. (2012), and Li and Carbone (2012). Li and Carbone (2012) concluded from a 4-yr satellite dataset that there was a positive statistical relationship between an increase in the local SST gradient, local low-level convergence, and rainfall initiation over the western Pacific warm pool. We find a similar correlation in our model fields as indicated in Fig. 13 and Fig. 14 though it remains unclear whether this relationship stems from changes in either the SST magnitude or gradient in this nonlinear full-physics model run.

A model sensitivity run using fixed SST does clearly show, however, that the diurnal SST variation has a strong influence on the modeled fields (Fig. 14). Note, in particular, that the convective rainfall in the uncoupled run lacks the strong diurnal signal apparent in the coupled run. Similar trends are evident in other parameters including the surface convergence and domain-averaged kinetic energy. Comparison of the coupled and uncoupled grid-3 domain mean enthalpy flux during the first 3 days indicates the diurnal SST creates a $35\,W\,m^{-2}$ enthalpy flux, a 33% increase in the enthalpy flux from

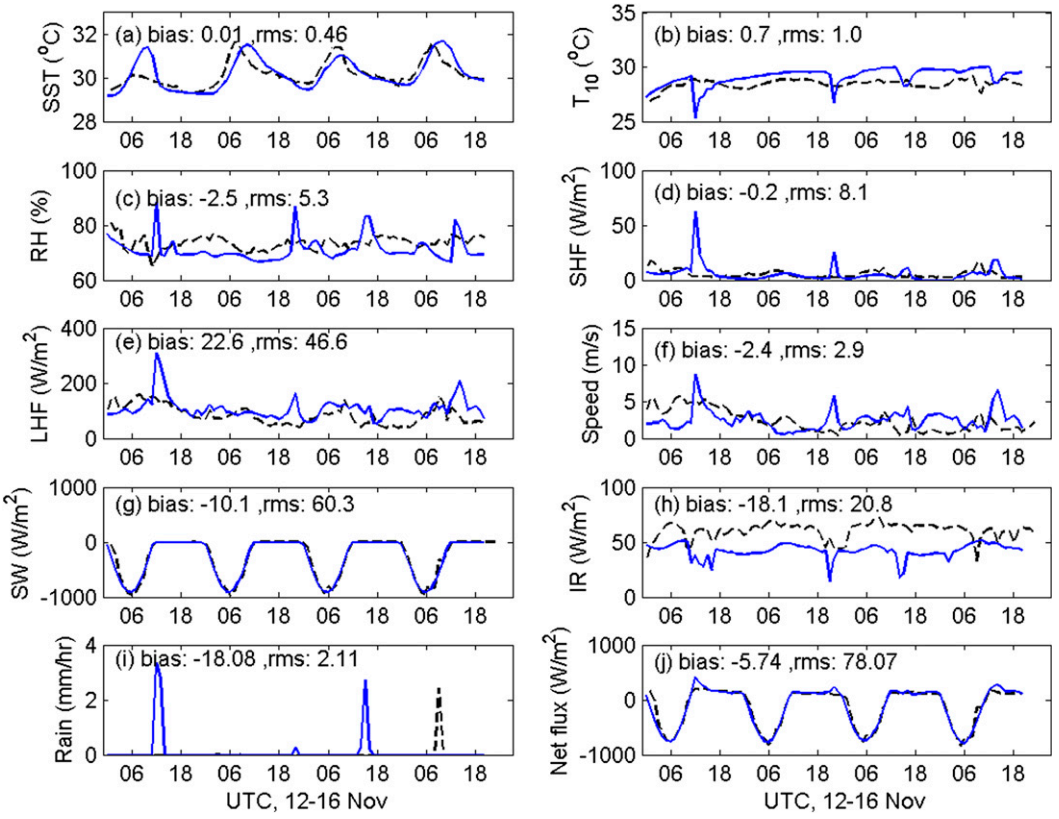

FIG. 10. Comparisons of *Revelle* (black) and COAMPS coupled simulation (blue) of (a) SST (°C), (b) 10-m air temperature (°C), (c) 10-m RH (%), (d) sensible heat flux (W m^{-2}), (e) latent heat flux (W m^{-2}), (f) 10-m wind speed (m s^{-1}), (g) shortwave radiation (W m^{-2}), (h) longwave radiation (W m^{-2}), (i) hourly precipitation (mm), and (j) net flux to the ocean (W m^{-2}). The bias (model − obs) and RMS values are displayed in each panel.

the cumulative effect of diurnal SST cycle, and nonlinear two-way coupling. This SST "pumping" leads to a 1.2% increase in the mean atmosphere TPW from 53.8 to 54.5 m, a 50% increase in column-integrated total mixing ratio (not shown), and a 44% increase in the grid-3 domain total precipitation. In the uncoupled experiment, the grid-3 domain mean low-level convergence was also decreased by 26% and may have effectively damped the subsequent increase of the atmosphere moisture, clouds, and precipitation in Fig. 14. These differences in the two model simulations thus provide insight to the questions posed in the introduction regarding the topic whether the atmospheric moistening during the suppressed phase of the MJO is modulated by the diurnal SST cycle.

One final aspect of the fully coupled COAMPS simulation regards the nature of the transition from a dry to moist environment in the MJO suppressed phase. A coarse look at this transition is obtained by displaying time–height plots of the grid-3 domainwide mean field values (Fig. 15). The vapor field, for example, reveals that the moisture increases occur both aloft between 5 and 10 km and between 0.5 and 2.5 km during the first two diurnal cycles covering the period from 12 to 14 November. This initial moisture increase, as revealed by the COAMPS perturbation diabatic heating from the cloud microphysical processes, is associated with the formation of convective towers and stratiform cloud layers that extend upward of 10 km from the surface. Diabatic cooling is near the melting level (near z = 5 km) and in association with the evaporation of rain and cloud water within the boundary layer. This evaporation coupled with additional surface fluxes help contribute to an increase in the near-surface relative humidity values below an elevation of approximately 1 km.

Subsequent growth of deeper and more vigorous convective towers tends to further deepen the moisture layer well above the 10-km level toward the end of the simulation after 15 November. This occurs with the transition to the easterly flow (Fig. 15), which is seen here to extend through a deep layer of the troposphere. This structure is suggestive of a passage of one or more large-scale waves during the second half of the

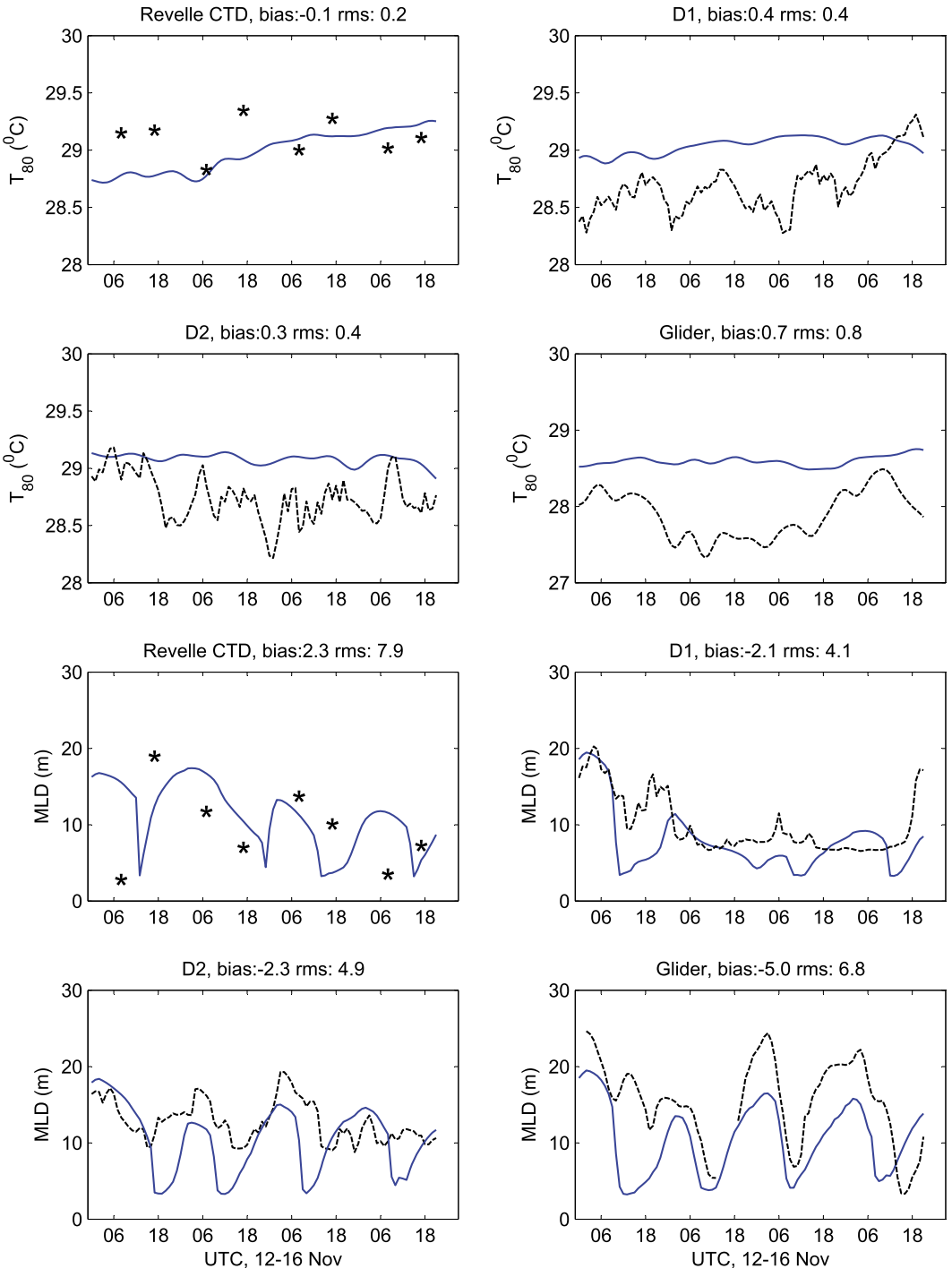

FIG. 11. Comparisons of COAMPS (blue) (first and second rows) vertically averaged temperature to 80-m depth and (third and fourth rows) mixed layer depth with *Revelle* (stars), D1, D2 and the sea glider (dashed black lines). The model bias (model − obs) and RMS fields are displayed on each panel.

simulation as previously indicated in Fig. 2. There is some suggestion in the model data of alternating bands of positive and negative meridional flow velocity that exhibit a westward tilt with height below an altitude of ~12 km. The strong positive v-component anomaly is particularly well defined and appears to be associated with a subtle local minimum in the RH values that extend through a deep layer of the troposphere.

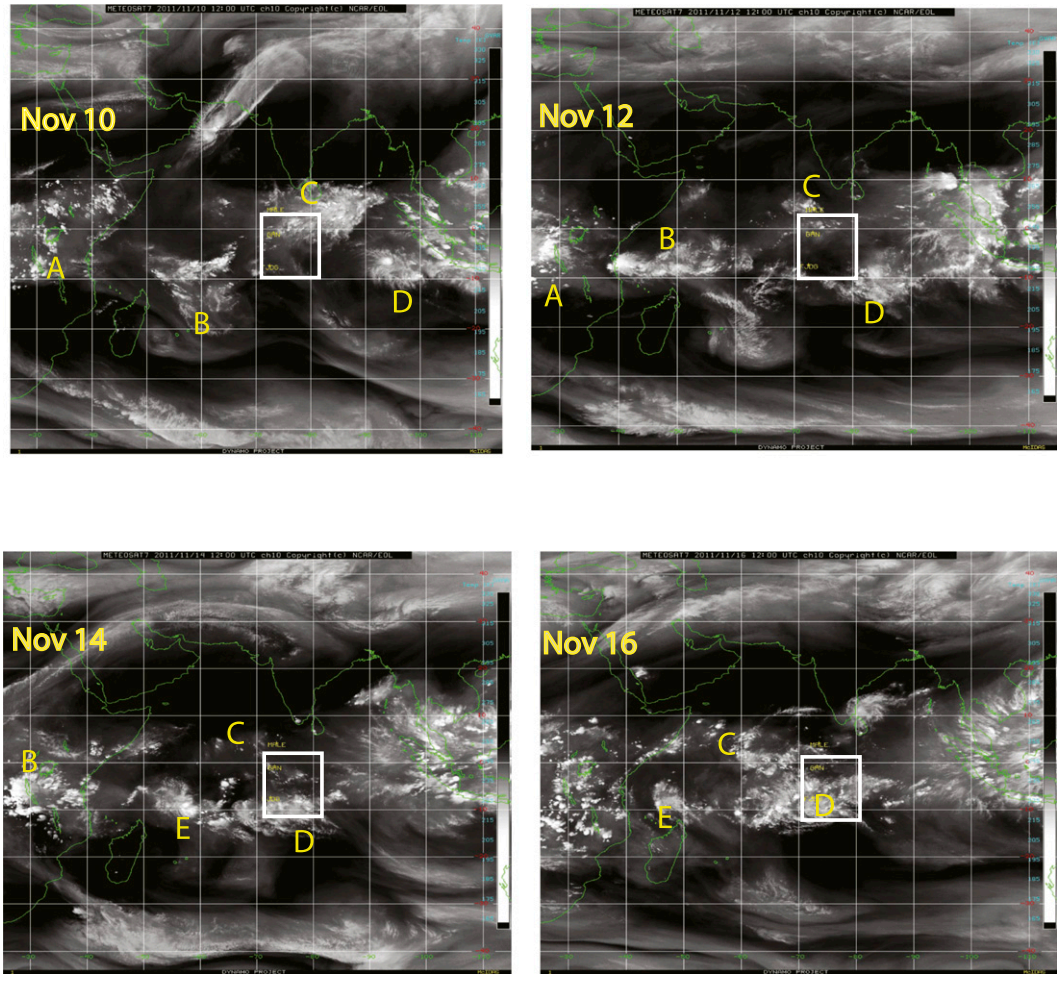

FIG. 12. *Meteosat-7* channel-10 water vapor images at 2-day intervals beginning at 1200 UTC 12 Nov through 1200 UTC 16 Nov 2011. The white lines are latitude and longitude increments of 10° each. The bold white box represents the COAMPS grid-3 domain. The bold letters A–E denote the primary convective cloud clusters observed during the period of interest covering the COAMPS forecasts described in the text. The convective regions C and D are seen to impact the northern and southern grid 3 of the COAMPS model domain.

b. Idealized COAMPS MRG wave simulation

The suggested presence of one or more large-scale waves over the last half of the COAMPS real-data simulation motivates a series of idealized experiments that were designed to further elucidate the possible role of such waves in the vapor resurgence evident in the observational and modeling data presented in the previous sections. In this initial study, we focus our attention on the structure of MRG waves and use the analytical forms of these waves described by Matsuno (1966) and Holton and Hakim (1979) to initialize a series of COAMPS model experiments in an effort to highlight the potential impact of the wave circulations on the structure and temporal evolution of the vapor field in a highly controlled experimental setup. An example of the simulated wave structure is first shown for the dry MRG wave (experiment EXPA) after 4 days of integration in Fig. 16. The figure reveals the familiar asymmetric perturbation velocity structure about the equator that decays exponentially toward both poles. The moisture field consists of a series of dry and moist mesoscale bands that extend well poleward of the equator in both hemispheres. The banded moisture anomalies are occurring in regions of the ascending and descending branches of the MRG circulation as well as regions of enhanced surface fluxes. The positive RH anomalies form a more continuous sinusoidal pattern that connects the separate maxima located in either hemisphere. This is similar to the positive anomalies in

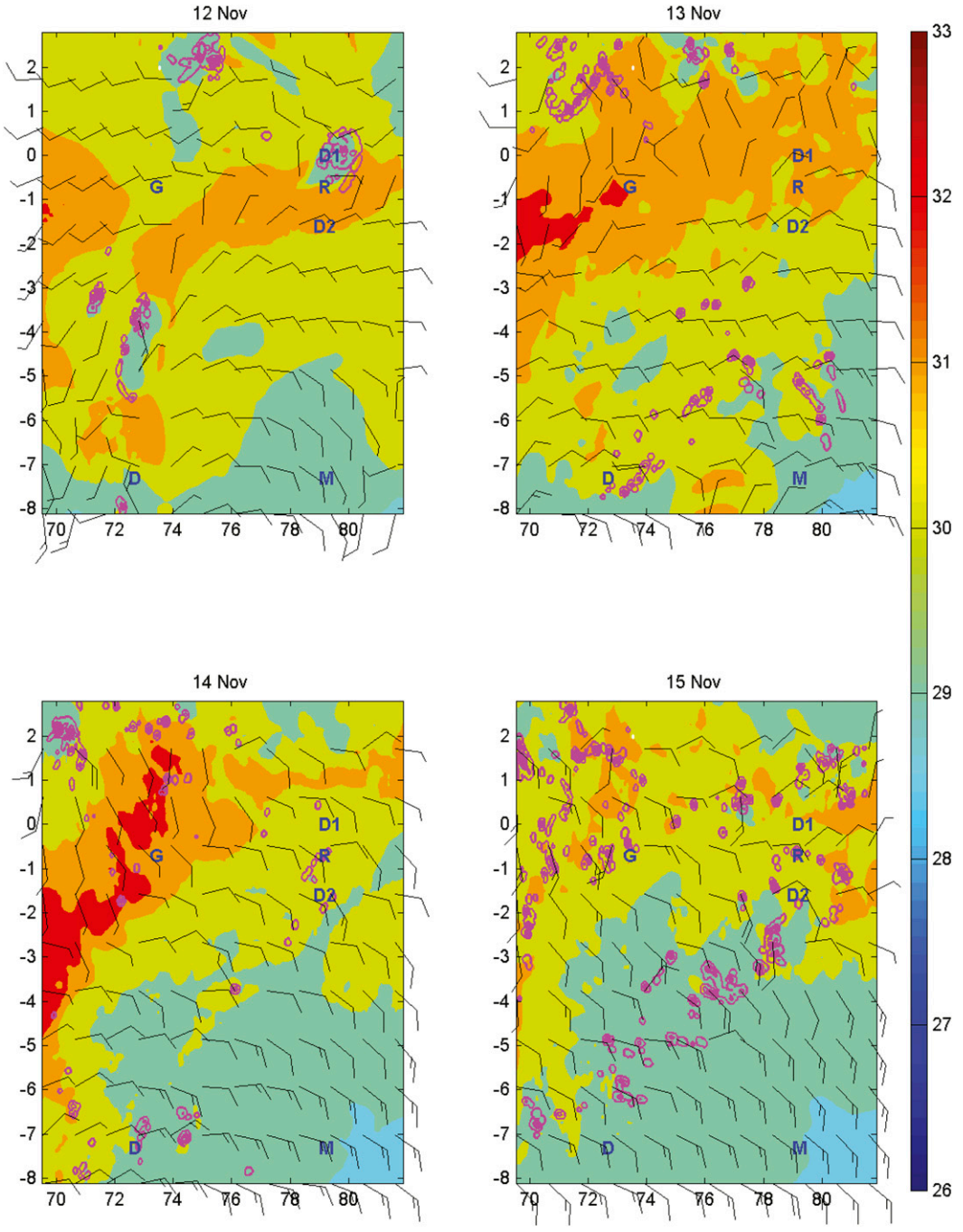

FIG. 13. COAMPS forecast of SST (color shaded), hourly rain rate (magenta contours), and 10-m winds (barbs) on the 3-km grid at 1200 UTC 12, 13, 14, and 15 Nov 2011. The SST contour interval is 1°C and the hourly rain rate contour is 10 mm h^{-1}. The zero contour is not plotted.

the zonal flow component, suggesting the development of an oscillating moist low-level zonal jet structure that straddles the equatorial region.

Mesoscale modulation in the moisture field is also evident in the vertical cross sections taken at a fixed latitude north of the equator (Fig. 17). The vertical RH structure exhibits a westward phase tilt with height as found to arise with the other perturbation fields shown. The RH maxima are clearly tied to that portion of the wave exhibiting the minimum temperature anomaly and are in quadrature with the vertical velocity field indicating a zero mean net vertical vapor transport when

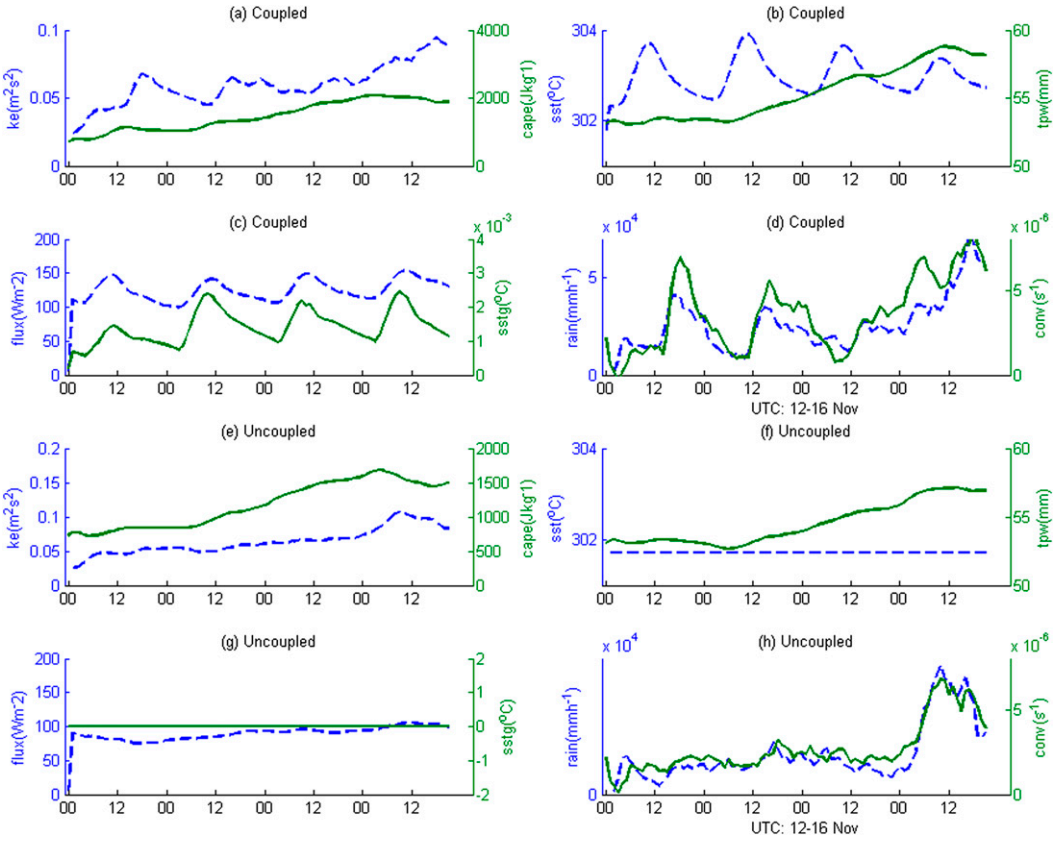

FIG. 14. Time series plots of coupled COAMPS grid-3 domain mean (a) kinetic energy ($m^2 s^{-2}$) and CAPE ($J kg^{-1}$), (b) SST (°C) and total precipitable water (mm), (c) enthalpy flux ($W m^{-2}$) and absolute magnitude of SST gradient (°C 9 km^{-2}), (d) domain total precipitation ($mm h^{-1}$) and domain mean low-level convergence (s^{-1}), and (e),(f) as in (a)–(d) except for the uncoupled COAMPS.

averaged across a wavelength. A time–height plot of the MRG taken from a fixed location north of the equator clearly illustrates a downward phase propagation of the various parameters in time with the phase relationships of the initial wave field well maintained throughout the entire duration of the 4-day forecast period. The vapor structure obtained at the time–height cross section shown in Fig. 17 in the sensitivity experiment that contains the diurnal SST fluctuation (EXPB) is similar to that of the control (EXPA) except that the boundary moisture values are higher by nearly 7 $g kg^{-1}$ (not shown). The additional inclusions of the full-physics sensitivity run (EXPC) acts to dry the boundary layer and increase the vapor aloft through convective transport.

Subtle changes in the vertical wave structure are seen in EXPC as the modeled convection begins to alter the vertical structure through a drying of the boundary layer and moistening of the upper troposphere. The onset of the model convection increases after 60 h of simulation when the MRG-induced cool and moist thermal anomaly in Fig. 18 is present over the lower 6 km of the atmosphere and the SST are reaching a peak value from the imposed diurnal cycle (between 72 and 84 h). Overall, the temporal change in the TPW from the initial value of 50 mm was on the order of 9%–13% for the three experiments (54.7, 56.4, and 56.3 mm, for experiments EXPA, EXPB, and EXPC, respectively) with the maximum change found to arise in the experiments including the SST cycling.

The 96-h mean moisture budget profile from EXPA taken at this same point illustrates the relative contribution of the various terms impacting the model vapor structure (Fig. 19). The vapor structure at low levels is clearly dominated by the turbulent mixing within the developing boundary layer. At low levels this term is aided by a small contribution from the horizontal advection and more strongly opposed by the low-level subsidence experienced at this particular point in the wave life cycle. The mixing term quickly damps with height, however, leaving a balance between the vertical and horizontal advection terms throughout the remainder of the troposphere. The oscillatory nature of

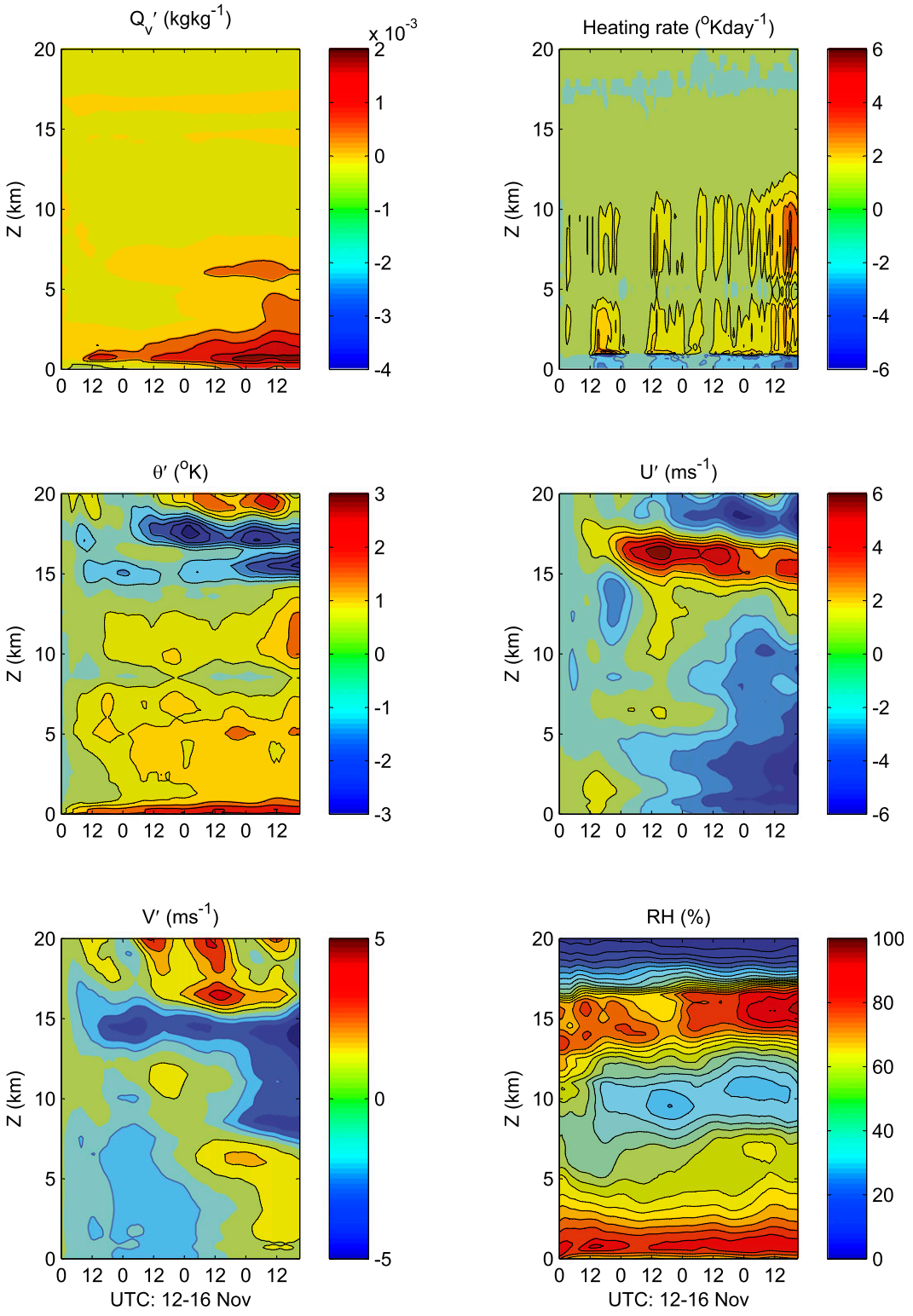

FIG. 15. Time–height cross section of the COAMPS grid-3 domain-averaged perturbation mixing ratio [Q_v'(kg kg^{-1})], diabatic heating (K day^{-1}), perturbation potential temperature [θ' (K)], perturbation zonal [U'] and meridional [V'] velocity components (m s^{-1}), and relative humidity RH (%) with respect to ice ($T < 273$ K) and water ($T > 273$ K). The abscissa on each plot represents the time starting at 0000 UTC 12 Nov 2011. The perturbations are computed from the domain mean values at each model level.

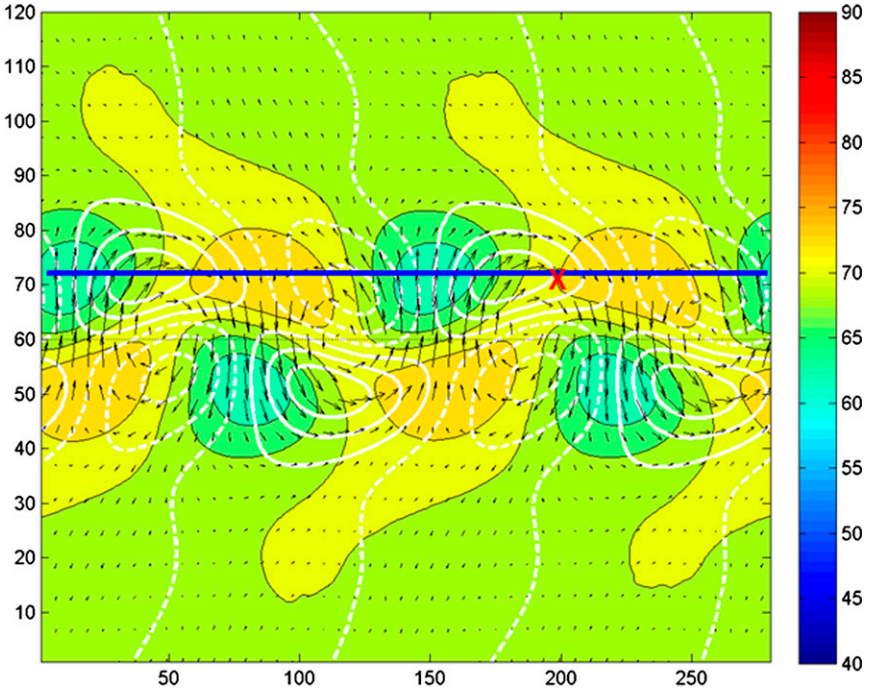

FIG. 16. A horizontal plan view of the idealized MRG structure taken at 96 h into the simulation at an elevation of 1.6 km for the idealized MRG control experiment (EXPA). The shaded field is relative humidity with respect to liquid water (%) and is contoured (black curves) at intervals of 2.5%. The positive (solid) and negative (dashed) u component of the flow is contoured in white at intervals of 0.5 m s^{-1}. The horizontal flow vectors are depicted by the black arrows. The displayed domain is 280 × 120 with $\Delta x = \Delta y = 0.5°$. The equator is indicated by the dashed line at the position $y = 60$. The MRG is moving from right to left at ~15 m s^{-1}. The bold blue line at $y = 72$ denotes the position of the vertical cross section shown in Fig. 17. The bold red cross shown at $y = 72$ and $x = 195$ represents the position of the time–height plot shown in Fig. 18 and the moisture budget analysis shown in Fig. 19.

these two remaining terms is apparent with height with the net trending toward zero aloft.

c. *The MRG waves and SST coupling mechanism*

The westward propagating MRG waves north of the equator and their hypothesized impact on the flow field, vapor, and cloud structure during the suppressed phase of the CINDY/DYNAMO MJO cycle are summarized as follows. The phase lines of the various state variables tilt westward with height initially and exhibit a downward phase propagation in time. The maximum RH values are found to correspond to the minimum in the thermal perturbation at the point where the vertical velocity changes sign from positive to negative values and are further noted to correspond to equatorward meridional flow. The opposite situation arises in the intervening dry zones, which are found to consist of a poleward flow component. The correlation between mean meridional fluxes of $\overline{v'q'}$ and $\overline{v'\theta'}$ associated with the MRG circulation is thus inferred to cool the equatorial region [as noted previously by Holton and Hakim (1979)] as well as to moisten it. The moistening resulting from the meridional eddy flux term $(-\partial\overline{v'q'_v}/\partial y)$ extends through a deep layer of the atmosphere within a 10° latitude belt centered at the equator and reaches a peak magnitude of ~0.25 g kg^{-1} day^{-1} for the conditions simulated in the dry idealized experiment EXPA (not shown). Perhaps significantly, this term in the dry experiments is seen to result in a symmetric moistening tendency about the equator. The symmetric nature of this forcing stands in contrast to the convective forcing itself, which exhibited a distinct asymmetric pattern about the equator as commonly found in observational studies of MRG waves (cf. Kiladis et al. 2009).

The deepest convective development in the moist experiments was shown to occur in regions of the MRG-induced maximum surface convergence and upper-tropospheric divergence as noted to occur here and in previous studies of convectively coupled MRG

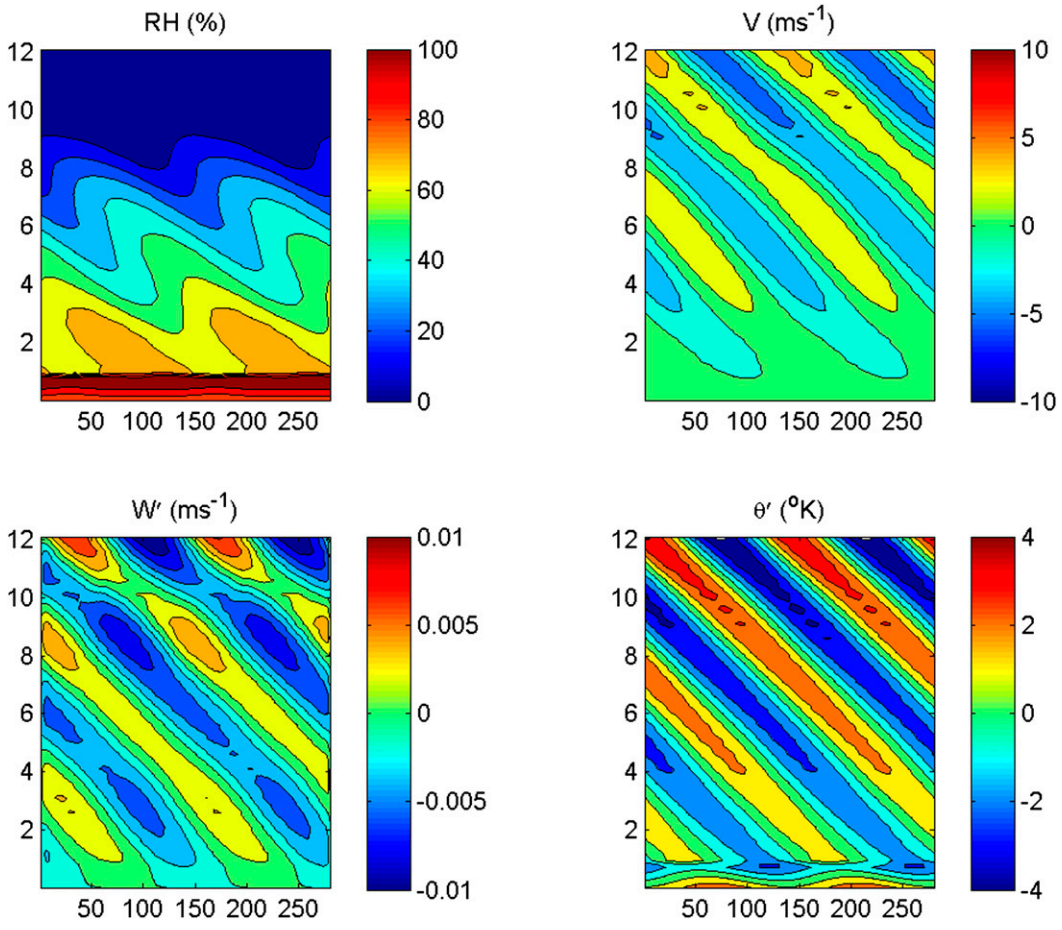

FIG. 17. A vertical x–z cross section of the idealized MRG structure taken at 96 h into the EXPA taken at a position just north of the equator ($y = 72$) in the plan view shown in Fig. 16. The displayed fields include the relative humidity (shaded and contoured every 10%), the perturbation v component of the flow (shaded and contoured every 1.0 m s^{-1}), the perturbation vertical velocity (shaded and contoured every 0.0025 m s^{-1}), and the potential temperature perturbation (shaded and contoured every 1 K). Note the pronounced westward tilt with height of all displayed parameters and the variation in depth of the boundary layer tied to fluctuations in w'. The abscissa values represent the model's x-dimension grid number while the ordinate represents height (km).

waves. Because of the nature of the vertical wave structure in these simulations, the deepest convection also appeared to arise when the deep layer of cooling associated with MRG uplift was situated in the middle troposphere. The intervening warm dry layer associated with the MRG-induced subsidence is envisioned to inhibit weaker convective elements leading to shallower cloud elements, which would be expected to detrain their moisture in the lower troposphere where the air aloft is anomalously warm and dry. Peak SST values are expected to arise immediately to the west of the maximum surface convergence and beneath the lower-tropospheric warm anomaly where deeper convective cloud development is suppressed. This contributes to the rise within the boundary layer vapor values near the region of maximum surface convergence.

6. Summary

Observations and model experiments were presented and used to investigate the resurgence of the deep layers of atmospheric moisture during the CINDY/DYNAMO MJO suppressed phase. Spectral density and wavelet analysis of the DYNAMO soundings, TRMM satellite precipitation, and DYNMO moorings showed the resurgence of moisture is tightly coupled with the ocean and occurs in a reoccurring fashion that includes diurnal, quasi-2-, quasi-3–4, quasi-6–8-, and quasi-16-day oscillations. To investigate processes that govern the resurgence of moisture, COAMPS model experiments were conducted between 12 and 16 November 2011, during which the environment started to transition back to a moist state from a post MJO1 dry phase. It is found

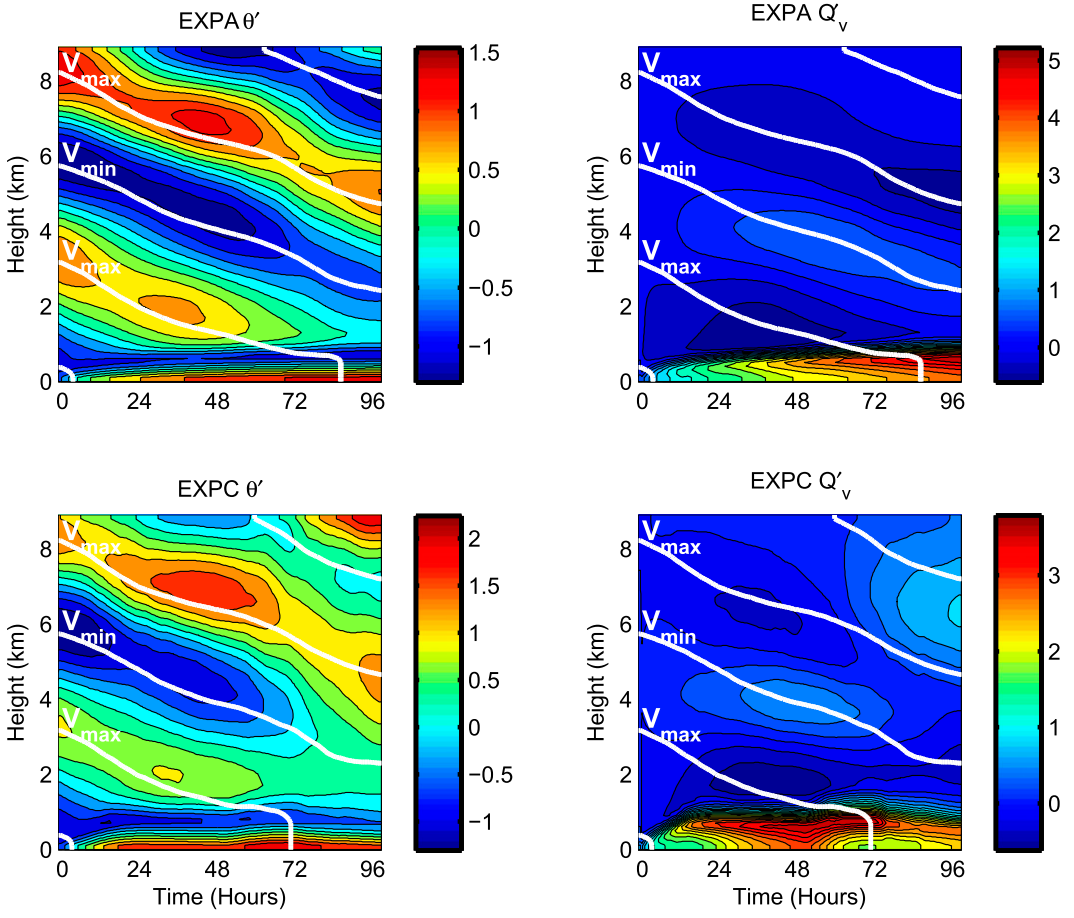

FIG. 18. A time–height cross section of the 96-h idealized MRG structure from experiment (top) EXPA simulation and (bottom) EXPC taken at a fixed located just north of the equator given by the bold red cross depicted in Fig. 16. The shading represents (left) the perturbation potential temperature (°C) and (right) perturbation mixing ratio ($g\,kg^{-1}$). The bold white curves denote the max–min phase lines of the perturbation meridional flow ($m\,s^{-1}$). Note the downward phase propagation of the maxima and minima in time and change in vapor structure in the boundary layer between EXPA and EXPC. The values along the abscissa represent the elapsed time (hours) from the start of the simulation while the ordinate represents height in km.

that air–sea interaction and the passage of MRG waves play an important role in the resurgence of moisture during this period. The COAMPS real-data results showed inclusion of the diurnal SST increased the TPW by 1.2% from the cumulative effect of diurnal SST cycle and nonlinear two-way air–sea interaction.

Further attempts to estimate the moisture increase during this period from diurnal SST pumping or induced by MRG or from both mechanisms is formulated in COAMPS idealized MRG experiments. These idealized experiments show that the TPW increase from the moisture transport of the dry MRG circulation is on the order of 9%. Superimposing a diurnal SST variation of 2.5°C as in the observed diurnal cycle further increased the TPW change to 13%. A similar value was found to occur with the full-physics MRG run that included a diurnal SST fluctuation and the coupling between the convection and SST. Further quantification of these impacts in the real atmosphere will require a greater range of simulations than explored here in order to account for differences in the observed diurnal SST and MRG characteristics from case to case.

Our observation analysis and modeling results generally agree with the recharge–discharge theory for MJO initiation first proposed by Hendon and Liebmann (1990) and Bladé and Hartmann (1993). Based on the above analysis of the moisture resurgence processes examined to occur during the CINDY/DYNAMO MJO suppressed phase, we propose an extension of the recharge–discharge theory to include the effect of diurnal SST variation and water vapor transport associated with the passage of large-scale transient waves.

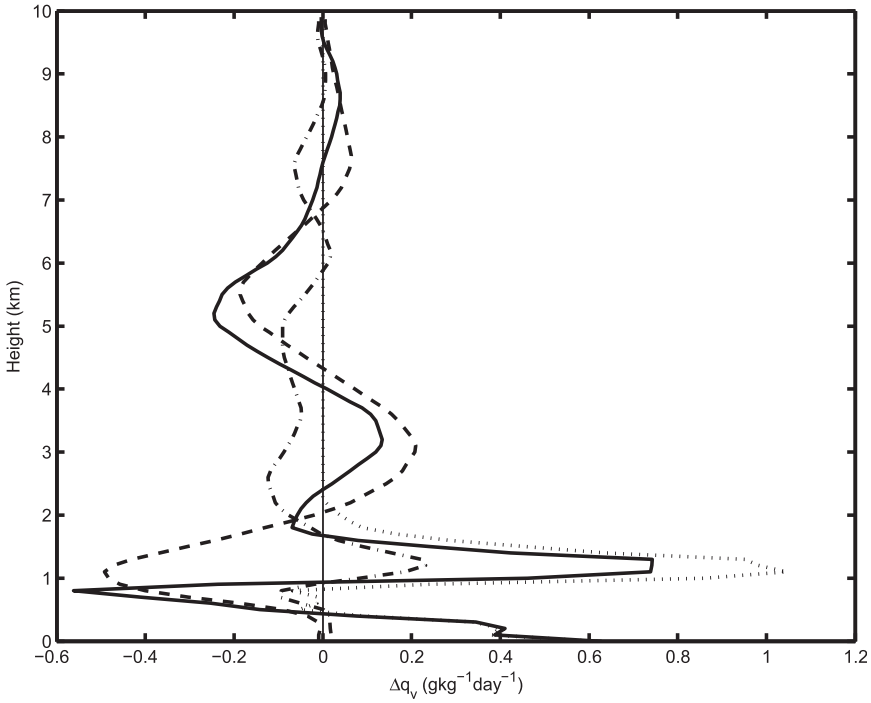

FIG. 19. A vertical profile of the EXPA 96-h mean water vapor budget (g kg^{-1} day^{-1}) for the budget point illustrated by the bold cross that was shown previously in Fig. 16. The total budget term (black line) includes the three largest leading terms from the vertical advection (dashed line), horizontal advection (dashed–dotted line), and vertical mixing (dotted line).

Our results are consistent with previous studies that the vapor resurgence during CINDY/DYNAMO MJO suppressed phase is a complex multiscale problem. Additional high-resolution cloud-resolving coupled model studies can help to advance the understanding of the moist resurgence process prior to the MJO initiation as well as their coupling with transient large-scale waves. Future work is planned to extend the idealized COAMPS simulations to include a full coupling between the ocean and velocity perturbations associated with inertio-gravity, Rossby, or Kelvin wave solutions in an effort to further isolate their contribution to the vapor resurgence during the MJO suppressed phase.

Acknowledgments. We thank Scot Loehrer of National Center for Atmospheric Research (NCAR) for assistance in acquiring the DYNAMO data. The sounding data was provided by NCAR/EOL under sponsorship of the National Science Foundation (http://data.eol.ucar.edu/). We appreciate Prof. James Moum for providing the *Revelle* CTD data. Appreciation extends to Gilbert Compo for helpful discussions on the use of wavelet analysis. Thanks go to anonymous reviewers for helpful review of the manuscript. This research is supported by the Office of Naval Research under Program Element 601153N and partially supported by NOAA CPO ESS program. The computing resource used for the real-time CINDY2011/DYNAMO COAMPS forecast and subsequent COAMPS MJO studies are provided by the Department of Defense High Performance Computing.

REFERENCES

Benedict, J. J., and D. A. Randall, 2007: Observed characteristics of the MJO relative to maximum rainfall. *J. Atmos. Sci.*, **64**, 2332–2354, doi:10.1175/JAS3968.1.

Berkelhammer, M., C. Risi, N. Kurita, and D. C. Noone, 2012: The moisture source sequence for the Madden-Julian Oscillation as derived from satellite retrievals of HDO and H_2O. *J. Geophys. Res.*, **117**, D03106, doi:10.1029/2011JD016803.

Bladé, I., and D. L. Hartmann, 1993: Tropical intraseasonal oscillations in a simple nonlinear model. *J. Atmos. Sci.*, **50**, 2922–2939, doi:10.1175/1520-0469(1993)050<2922:TIOIAS>2.0.CO;2.

Chen, S., and Coauthors, 2003: COAMPS version 3 model description. NRL Publ. NRL/PU/7500-03-448, 143 pp.

——, T. J. Campbell, H. Jin, S. Gaberšek, R. M. Hodur, and P. Martin, 2010: Effect of two-way air–sea coupling in high and low wind speed regimes. *Mon. Wea. Rev.*, **138**, 3579–3602, doi:10.1175/2009MWR3119.1.

Ciesielski, P. E., P. T. Haertel, R. H. Johnson, J. Wang, and S. M. Loehrer, 2012: Developing high-quality field program

sounding datasets. *Bull. Amer. Meteor. Soc.*, **93**, 325–336, doi:10.1175/BAMS-D-11-00091.1.

Fairall, C. W., E. F. Bradley, J. E. Hare, A. A. Grachev, and J. B. Edson, 2003: Bulk parameterization of air–sea fluxes: Updates and verification for the COARE algorithm. *J. Climate*, **16**, 571–591, doi:10.1175/1520-0442(2003)016<0571:BPOASF>2.0.CO;2.

Flatau, M., P. J. Flatau, P. Phoebus, and P. P. Niiler, 1997: The feedback between equatorial convection and local radiative and evaporative processes: The implications for intraseasonal oscillations. *J. Atmos. Sci.*, **54**, 2373–2386, doi:10.1175/1520-0469(1997)054<2373:TFBECA>2.0.CO;2.

Frenger, I., N. Gruber, R. Knutti, and M. Münnich, 2013: Imprint of Southern Ocean eddies on winds, clouds and rainfall. *Nat. Geosci.*, **6**, 608–612, doi:10.1038/ngeo1863.

Gottschalck, J., P. E. Roundy, C. J. Schreck III, A. Vintzileos, and C. Zhang, 2013: Large-scale atmospheric and oceanic conditions during the 2011–12 DYNAMO field campaign. *Mon. Wea. Rev.*, **141**, 4173–4196, doi:10.1175/MWR-D-13-00022.1.

Hendon, H. H., and B. Liebmann, 1990: The intraseasonal (30–50 day) oscillation of the Australian summer monsoon. *J. Atmos. Sci.*, **47**, 2909–2924, doi:10.1175/1520-0469(1990)047<2909:TIDOOT>2.0.CO;2.

——, and ——, 1991: The structure and annual variation of antisymmetric fluctuations of tropical convection and their association with Rossby–gravity waves. *J. Atmos. Sci.*, **48**, 2127–2140, doi:10.1175/1520-0469(1991)048<2127:TSAAVO>2.0.CO;2.

Hodur, R. M., 1997: The Naval Research Laboratory's Coupled Ocean/Atmosphere Mesoscale Prediction System (COAMPS). *Mon. Wea. Rev.*, **125**, 1414–1430, doi:10.1175/1520-0493(1997)125<1414:TNRLSC>2.0.CO;2.

Holton, J. R., and G. J. Hakim, 1979: *An Introduction to Dynamic Meteorology*. 2nd ed. Academic Press, 391 pp.

Hsu, H.-H., B. J. Hoskins, and F.-F. Jin, 1990: The 1985/86 intraseasonal oscillation and the role of the extratropics. *J. Atmos. Sci.*, **47**, 823–839, doi:10.1175/1520-0469(1990)047<0823:TIOATR>2.0.CO;2.

Jensen, T. G., T. J. Campbell, R. A. Allard, R. J. Small, and T. A. Smith, 2011: Turbulent heat fluxes during an intense cold-air outbreak over the Kuroshio Extension Region: Results from a high-resolution coupled atmosphere–ocean model. *Ocean Dyn.*, **61**, 657–674, doi:10.1007/s10236-011-0380-0.

Johnson, R. H., and P. E. Ciesielski, 2013: Structure and properties of Madden–Julian oscillations deduced from DYNAMO sounding arrays. *J. Atmos. Sci.*, **70**, 3157–3179, doi:10.1175/JAS-D-13-065.1.

Kemball-Cook, S., and B. Wang, 2001: Equatorial waves and air–sea interaction in the boreal summer intraseasonal oscillation. *J. Climate*, **14**, 2923–2942, doi:10.1175/1520-0442(2001)014<2923:EWAASI>2.0.CO;2.

Kiladis, G. N., M. C. Wheeler, P. T. Haertel, K. H. Straub, and P. E. Roundy, 2009: Convectively coupled equatorial waves. *Rev. Geophys.*, **47**, RG2003, doi:10.1029/2008RG000266.

Kurita, N., D. Noone, C. Risi, G. Schmidt, H. Yamada, and K. Yoneyama, 2011: Intraseasonal isotopic variation associated with the Madden-Julian Oscillation. *J. Geophys. Res.*, **116**, D24101, doi:10.1029/2010JD015209.

Lau, W. K.-M., and L. Peng, 1987: Origin of low-frequency (intraseasonal) oscillations in the tropical atmosphere. Part I: The basic theory. *J. Atmos. Sci.*, **44**, 950–972, doi:10.1175/1520-0469(1987)044<0950:OOLFOI>2.0.CO;2.

——, and D. E. Waliser, Eds., 2005: *Intraseasonal Variability of the Atmosphere-Ocean Climate System*. Springer, 474 pp.

Li, Y., and R. E. Carbone, 2012: Excitation of rainfall over the tropical western Pacific. *J. Atmos. Sci.*, **69**, 2983–2994, doi:10.1175/JAS-D-11-0245.1.

Lindzen, R. S., 1974: Wave-CISK in the tropics. *J. Atmos. Sci.*, **31**, 156–179, doi:10.1175/1520-0469(1974)031<0156:WCITT>2.0.CO;2.

Lynch, P., and X. Y. Huang, 1992: Initialization of the HIRLAM model using a digital filter. *Mon. Wea. Rev.*, **120**, 1019–1034, doi:10.1175/1520-0493(1992)120<1019:IOTHMU>2.0.CO;2.

Madden, R., and P. Julian, 1971: Detection of a 40–50-day oscillation in the zonal wind in the tropical Pacific. *J. Atmos. Sci.*, **28**, 702–708, doi:10.1175/1520-0469(1971)028<0702:DOADOI>2.0.CO;2.

——, and ——, 1972: Description of global-scale circulation cells in the tropics with a 40–50-day period. *J. Atmos. Sci.*, **29**, 1109–1123, doi:10.1175/1520-0469(1972)029<1109:DOGSCC>2.0.CO;2.

Maloney, E. D., 2009: The moist static energy budget of a composite tropical intraseasonal oscillation in a climate model. *J. Climate*, **22**, 711–729, doi:10.1175/2008JCLI2542.1.

——, and D. L. Hartmann, 2000: Modulation of eastern North Pacific hurricanes by the Madden–Julian oscillation. *J. Climate*, **13**, 1451–1460, doi:10.1175/1520-0442(2000)013<1451:MOENPH>2.0.CO;2.

Martin, P. J., 2000: A description of the Navy Coastal Ocean model version 1.0. NRL Rep. NRL/FR/7322-00-9962, Naval Research Laboratory, Stennis Space Center, 42 pp. [Available online http://www.dtic.mil/cgi-bin/GetTRDoc?Location=U2&doc=GetTRDoc.pdf&AD=ADA387444.]

Matsuno, T., 1966: Quasi-geostrophic motions in the equatorial area. *J. Meteor. Soc. Japan*, **44**, 25–43.

O'Neill, L. W., D. B. Chelton, and S. K. Esbensen, 2012: Covariability of surface wind and stress responses to sea surface temperature fronts. *J. Climate*, **25**, 5916–5942, doi:10.1175/JCLI-D-11-00230.1.

Pan, H.-L., and W.-S. Wu, 1995: Implementing a mass flux convection parameterization package for the NMC medium-range forecast model. NMC Office Note 409, 40 pp.

Powell, S. W., and R. A. Houze, 2013: The cloud population and onset of the Madden-Julian Oscillation over the Indian Ocean during DYNAMO-AMIE. *J. Geophys. Res. Atmos.*, **118**, 11 979–11 995, doi:10.1002/2013JD020421.

Price, J. F., 2009: Metrics of hurricane-ocean interaction: Vertically-integrated or vertically-averaged ocean temperature? *Ocean Sci. Discuss.*, **6**, 909–951, doi:10.5194/osd-6-909-2009.

Raymond, D. J., and D. J. Torres, 1998: Fundamental moist modes of the equatorial troposphere. *J. Atmos. Sci.*, **55**, 1771–1790, doi:10.1175/1520-0469(1998)055<1771:FMMOTE>2.0.CO;2.

——, and Ž. Fuchs, 2009: Moisture modes and the Madden–Julian oscillation. *J. Climate*, **22**, 3031–3042, doi:10.1175/2008JCLI2739.1.

Roundy, P. E., 2008: Analysis of convectively coupled Kelvin waves in the Indian Ocean MJO. *J. Atmos. Sci.*, **65**, 1342–1359, doi:10.1175/2007JAS2345.1.

Seo, K.-H., and K.-Y. Kim, 2003: Propagation and initiation mechanism of the Madden-Julian oscillation. *J. Geophys. Res.*, **108**, 4384, doi:10.1029/2002JD002876.

Shinoda, T., H. H. Hendon, and J. Glick, 1998: Intraseasonal variability of surface fluxes and sea surface temperature in the tropical western Pacific and Indian Oceans. *Climate*, **11**, 1685–1702, doi:10.1175/1520-0442(1998)011<1685:IVOSFA>2.0.CO;2.

——, T. Jensen, M. Flatau, and S. Chen, 2013: Surface wind and upper-ocean variability associated with the Madden–Julian oscillation simulated by the Coupled Ocean–Atmosphere

Mesoscale Prediction System (COAMPS). *Mon. Wea. Rev.*, **141**, 2290–2307, doi:10.1175/MWR-D-12-00273.1.

Small, R. J., T. Campbell, J. Teixeira, S. Carniel, T. A. Smith, J. Dykes, S. Chen, and R. Allard, 2011: Air–sea interaction in the Ligurian Sea: Assessment of a coupled ocean–atmosphere model using in situ data from LASIE07. *Mon. Wea. Rev.*, **139**, 1785–1808, doi:10.1175/2010MWR3431.1.

Smith, T. A., and Coauthors, 2013: Ocean–wave coupled modeling in COAMPS-TC: A study of Hurricane Ivan (2004). *Ocean Modell.*, **69**, 181–194, doi:10.1016/j.ocemod.2013.06.003.

Sobel, A., and E. Maloney, 2013: Moisture modes and the eastward propagation of the MJO. *J. Atmos. Sci.*, **70**, 187–192, doi:10.1175/JAS-D-12-0189.1.

Sperber, K. R., 2003: Propagation and the vertical structure of the Madden–Julian oscillation. *Mon. Wea. Rev.*, **131**, 3018–3037, doi:10.1175/1520-0493(2003)131<3018:PATVSO>2.0.CO;2.

Takayabu, Y. N., K.-M. Lau, and C.-H. Sui, 1996: Observation of a quasi-2-day wave during TOGA COARE. *Mon. Wea. Rev.*, **124**, 1892–1913, doi:10.1175/1520-0493(1996)124<1892:OOAQDW>2.0.CO;2.

Tian, B., D. E. Waliser, E. J. Fetzer, and Y. L. Yung, 2010: Vertical moist thermodynamic structure of the Madden–Julian oscillation in atmospheric infrared sounder retrievals: An update and a comparison to ECMWF Interim Re-Analysis. *Mon. Wea. Rev.*, **138**, 4576–4582, doi:10.1175/2010MWR3486.1.

Torrence, C., and G. P. Compo, 1998: A practical guide to wavelet analysis. *Bull. Amer. Meteor. Soc.*, **79**, 61–78, doi:10.1175/1520-0477(1998)079<0061:APGTWA>2.0.CO;2.

Waliser, D. E., K.-M. Lau, and J.-H. Kim, 1999: The influence of coupled sea surface temperatures on the Madden–Julian oscillation: A model perturbation experiment. *J. Atmos. Sci.*, **56**, 333–358, doi:10.1175/1520-0469(1999)056<0333:TIOCSS>2.0.CO;2.

Wang, B., and H. Rui, 1990: Synoptic climatology of transient tropical intraseasonal convection anomalies: 1975–1985. *Meteor. Atmos. Phys.*, **44**, 43–61, doi:10.1007/BF01026810.

——, and X. Xie, 1998: Coupled modes of the warm pool climate system. Part I: The role of the air–sea interaction in maintaining the Madden–Julian oscillation. *J. Climate*, **11**, 2116–2135, doi:10.1175/1520-0442-11.8.2116.

Weare, B. C., 2003: Composite singular value decomposition analysis of moisture variations associated with the Madden–Julian oscillation. *J. Climate*, **16**, 3779–3792, doi:10.1175/1520-0442(2003)016<3779:CSVDAO>2.0.CO;2.

Wheeler, M., and G. N. Kiladis, 1999: Convectively coupled equatorial waves: Analysis of clouds and temperature in the wavenumber–frequency domain. *J. Atmos. Sci.*, **56**, 374–399, doi:10.1175/1520-0469(1999)056<0374:CCEWAO>2.0.CO;2.

——, and H. H. Hendon, 2004: An all-season real-time multivariate MJO index: Development of an index for monitoring and prediction. *Mon. Wea. Rev.*, **132**, 1917–1932, doi:10.1175/1520-0493(2004)132<1917:AARMMI>2.0.CO;2.

Yang, G.-Y., B. Hoskins, and J. Slingo, 2003: Convectively coupled equatorial waves: A new methodology for identifying wave structures in observational data. *J. Atmos. Sci.*, **60**, 1637–1654, doi:10.1175/1520-0469(2003)060<1637:CCEWAN>2.0.CO;2.

Yasunaga, K., K. Yoneyama, Q. Moteki, M. Fujita, Y. N. Takayabu, J. Suzuki, T. Ushiyama, and B. Mapes, 2010: Characteristics of 3–4- and 6–8-day period disturbances observed over the tropical Indian Ocean. *Mon. Wea. Rev.*, **138**, 4158–4174, doi:10.1175/2010MWR3469.1.

Yoneyama, K., C. Zhang, and C. Long, 2013: Tracing pulses of the Madden–Julian oscillation. *Bull. Amer. Meteor. Soc.*, **94**, 1871–1891, doi:10.1175/BAMS-D-12-00157.1.

Zhang, C., 2005: Madden-Julian Oscillation. *Rev. Geophys.*, **43**, RG2003, doi:10.1029/2004RG000158.